

**Influence of nitrogen oxides and volatile organic compounds emission changes on  
tropospheric ozone variability, trends and radiative effect**

Suvarna Fadnavis<sup>1</sup>, Yasin Elshorbany<sup>2</sup>, Jerald Ziemke<sup>3</sup>, Brice Barret<sup>4</sup>, Alexandru Rap<sup>5</sup>, PR  
Satheesh Chandran<sup>1</sup>, Richard J. Pope<sup>6</sup>, Vijay Sagar<sup>1</sup>, Domenico Taraborrelli<sup>7</sup>, Eric Le  
Flochmoen<sup>4</sup>, Juan Cuesta<sup>8</sup>, Catherine Wespes<sup>9</sup>, Folkert Boersma<sup>10,11</sup>, Isolde Glissenaar<sup>10</sup>,  
Isabelle De Smedt<sup>12</sup>, Michel Van Roozendael<sup>12</sup>, Hervé Petetin<sup>13</sup>, Isidora Anglou<sup>10</sup>

<sup>1</sup>Center for Climate Change Research, Indian Institute of Tropical Meteorology, MoES, Pune,  
India

<sup>2</sup>School of Geosciences, College of Arts and Sciences, University of South Florida, St.  
Petersburg, FL, USA

<sup>3</sup>NASA Goddard Space Flight Center, Greenbelt, Maryland, USA

<sup>4</sup>LAERO/OMP, Université Paul Sabatier, Université de Toulouse-CNRS, Toulouse, France

<sup>5</sup>School of Earth and Environment, University of Leeds, Leeds, UK;

<sup>6</sup>National Centre for Earth Observation, University of Leeds, Leeds, UK

<sup>7</sup>Institute of Climate and Energy Systems, ICE-3: Troposphere, Forschungszentrum Jülich  
GmbH, Jülich, Germany,

<sup>8</sup>University Paris Est Creteil and Université Paris Cité, CNRS, LISA, F-94010 Créteil, France

<sup>9</sup>Université libre de Bruxelles (ULB), Spectroscopy, Quantum Chemistry and Atmospheric  
Remote Sensing, Brussels, Belgium

<sup>10</sup>Royal Netherlands Meteorological Institute (KNMI), De Bilt, The Netherlands

<sup>11</sup>Wageningen University, Environmental Sciences Group, Wageningen, The Netherlands

<sup>12</sup>Belgian Institute for Space Aeronomy, Brussels, Belgium

<sup>13</sup>Barcelona Supercomputing Center, Barcelona, Spain

**Corresponding author email: suvarna@tropmet.res.in**

## Abstract

Ozone in the troposphere is a prominent pollutant whose production is sensitive to the emissions of nitrogen oxides (NO<sub>x</sub>) and volatile organic compounds (VOC). Here, we assess the variation of tropospheric ozone levels, trends, ozone photochemical regimes, and radiative effects using the ECHAM6–HAMMOZ chemistry-climate model for the period 1998–2019 and satellite measurements. The global mean simulated trend in Tropospheric Column Ozone (TRCO) for the study period (1998–2019) is 0.89 ppb decade<sup>-1</sup>. During the overlapping period with OMI/MLS observations (2005–2019), the simulated global mean TRCO trends (1.58 ppb decade<sup>-1</sup>) show fair agreement with OMI/MLS estimates (1.4 ppb decade<sup>-1</sup>). The simulations for doubling emissions of NO<sub>x</sub> (DoubNO<sub>x</sub>), VOCs (DoubVOC), halving of emissions NO<sub>x</sub> (HalfNO<sub>x</sub>) and VOCs (HalfVOC) show nonlinear responses to ozone trends and tropospheric ozone photochemical regimes. The DoubNO<sub>x</sub> simulations show VOC–limited regimes over Indo-Gangetic-Plains, Eastern-China, Western-Europe, and the Eastern-US, while HalfNO<sub>x</sub> simulations show NO<sub>x</sub>–limited regimes over North-America and Asia. Emissions changes in NO<sub>x</sub> (DoubNO<sub>x</sub>/HalfNO<sub>x</sub>) influence the shift in tropospheric ozone photochemical regimes compared to VOCs (DoubVOC/HalfVOC).

The estimated global mean TO3RE during 1998–2019 from the CTL simulations is 1.21 Wm<sup>-2</sup>. The global mean TO3RE shows enhancement by 0.36 W m<sup>-2</sup> in DoubNO<sub>x</sub> simulations than CTL. While TO3RE shows a reduction in other simulations compared to CTL (DoubVOC: -0.005 Wm<sup>-2</sup>; HalfNO<sub>x</sub>: -0.12 Wm<sup>-2</sup>; and HalfVOC: -0.03 Wm<sup>-2</sup>). We show that emissions changes in anthropogenic NO<sub>x</sub> cause higher changes in TO3RE than anthropogenic VOCs.

**Key words:** Tropospheric ozone, trends, ozone photochemical regimes; ozone radiative effect. FNR; ECHAM6-HAMMOZ model simulations.

## 1. Introduction

Tropospheric ozone, a major air pollutant, has been a pressing issue in recent decades due to its detrimental effect on human health and ecosystem productivity and as a short-term climate forcer (Riese et al. 2012; Gulev et al., 2021; Wang et al., 2022). Considering these harmful impacts, the assessment of tropospheric ozone levels and trends are being conducted frequently (Gaudel et al., 2018; Mills et al., 2018; Tarasick et al., 2019). Ozone trends are being assessed from surface observations, in-situ and ground-based measurements, satellite retrievals, and model simulations (Cooper et al., 2014; Cohen et al., 2018; Young et al., 2018; Tarasick et al., 2019; Archibald et al., 2020). The latest IPCC AR6 reported an enhancement in free tropospheric ozone by  $2 - 7\%$  decade<sup>-1</sup> in the northern mid-latitudes,  $2 - 12\%$  per decade in the tropics, and  $<5\%$  decade<sup>-1</sup> in southern mid-latitudes (Gulev et al., 2021; Szopa et al., 2021). The Tropospheric Ozone Assessment Reports (TOAR) have documented global increases of tropospheric column ozone (TRCO) in the 20th century (Cooper et al., 2014; Lefohn et al., 2017; Schultz et al., 2017; Fleming et al., 2018; Gaudel et al., 2018; Mills et al., 2018; Young et al., 2018; Tarasick et al., 2019). Increasing tropospheric trends are explained by enhanced anthropogenic emissions (Cooper et al., 2014; Zhang et al., 2016) and modulation by climate variability (Lin et al., 2014; Lu et al., 2018). Several studies have documented increasing trends in TRCO across various regions and different time periods.

For instance, enhancement in TRCO trends globally using measurements from multiple sources such as In-service Aircraft for a Global Observing System database (IAGOS) and ozonesondes and GEOS-Chem model simulation revealed an increasing trend of  $2.7 \pm 1.7$  and  $1.9 \pm 1.7$  ppb decade<sup>-1</sup> between 1995 and 2017 (Wang et al., 2022). Additionally, Fiore et al. (2022) also found increasing trends ranging from  $0.6$  to  $2.5$  ppb decade<sup>-1</sup> from 1950 to 2014 globally based on the available limited surface ozone records and the Community Earth System, version-2, the Whole Atmosphere Community Climate Model, version-6 (CESM2–WACCM6) model study. Furthermore, trends in TRCO are stronger in the Northern Hemisphere (NH) than Southern Hemisphere (SH) due to larger anthropogenic emissions (Monks et al., 2015). Ozone Monitoring Instrument (OMI) and Microwave Limb Sounder (MLS) observations from 2005 until 2010 show annual TRCO burden averaged over the NH exceeds the SH by 4% at low latitudes ( $0^\circ - 25^\circ$ ), by 12% at mid-latitudes ( $25^\circ - 50^\circ$ ), and by 18% at high latitudes ( $50^\circ - 60^\circ$ ) (Cooper et al., 2014). CMIP6 models also show that the

tropospheric ozone burden increased by 44 % in 2005 – 2014 compared to 1850 (Griffiths et al., 2021). Recently, studies have reported a decrease in TRCO trends globally after the Corona–Virus Disease 2019 (COVID–19) outbreak e.g., Chang et al. (2022, 2023), and Steinbrecht et al. (2021). Also, Putero et al. (2023) show widespread ozone decreases at high-elevation sites due to the COVID–19 lockdown. However, our study period (1998–2019) excludes the COVID–19 associated emission changes.

Nitrogen oxides (NO<sub>x</sub>; NO+NO<sub>2</sub>) and volatile organic compounds (VOC) are the major precursors that define ozone photochemical regimes (Duncan et al 2010). Information on ozone photochemical regimes is of utmost importance to know ozone (O<sub>3</sub>) levels. However, the non-linearity in the O<sub>3</sub> – NO<sub>x</sub> – VOC chemistry has always posed a challenge in identifying photochemical regimes. The regime is called NO<sub>x</sub>–limited if the ozone production is directly related to a change in NO<sub>x</sub> rather than from VOC perturbations. Whereas the region where ozone production is regulated by the ambient availability of VOCs is called VOC–limited (Sillman et al., 1990; Kleinman, 1994). The ratios such as ozone to oxidized nitrogen species (O<sub>3</sub>/(NO<sub>y</sub>-NO<sub>x</sub>), where NO<sub>y</sub> is the total reactive nitrogen), formaldehyde to total reactive nitrogen (HCHO/NO<sub>y</sub>), formaldehyde to nitrogen dioxide (HCHO/NO<sub>2</sub>), hydrogen peroxide to nitric acid (H<sub>2</sub>O<sub>2</sub>/HNO<sub>3</sub>) are adopted to diagnose the ozone photochemical regimes (e.g., Sillman, 1995; Martin et al., 2004; Duncan et al., 2010). Among these, the most widely used indicator to identify regimes is the Formaldehyde (HCHO) to Nitrogen dioxide (NO<sub>2</sub>) Ratio (FNR) (Martin et al., 2004; Duncan et al., 2010). In our study, we adopt FNR to identify NO<sub>x</sub>–limited or VOC–limited regimes. On par with the current effort to mitigate ozone pollution, it is important to understand how the changes in emissions of NO<sub>x</sub> and VOC affect the ozone photochemical regimes and trends (Jin et al., 2017, 2020).

Ozone is the third strongest anthropogenic greenhouse gas, also called a short-term climate forcer, producing a global average radiative forcing of 0.47 [0.24 to 0.71 W m<sup>-2</sup>] [5% to 95% uncertainty range] (Forster et al., 2021). Recent studies showed ozone effective radiative forcing (ERF) of 0.51 [0.25 to 0.76] W m<sup>-2</sup> during 1750 – 2023 (Forster et al., 2024). The knowledge of ozone radiative forcing due to changes in anthropogenic emissions of NO<sub>x</sub> and VOC will help to assess climate change. Therefore, we also show the impacts of enhanced or reduced emissions of NO<sub>x</sub> and VOC on ozone radiative effect in addition to ozone trends

and photochemical regimes. To achieve this, we conducted sensitivity experiments by doubling and halving global NO<sub>x</sub> and VOC emissions using the state-of-the-art chemistry-climate model ECHAM6–HAMMOZ for the period 1998–2019. This approach of increase/decrease of emissions is important to understand the nonlinear response of ozone to emission changes. These experiments are helpful for designing emission implementation strategies (e.g., Zhang et al., 2021; Wang et al., 2023). The paper is outlined as follows: satellite data and the model experimental setup are given in section 2, and results are given in section 3, which includes a comparison of simulated tropospheric column ozone with satellite data and estimated ozone trends. Discussions on ozone photochemical regimes and their trends are made in sections 4 to 6. Estimates of ozone radiative effects are given in section 7. Conclusions are made in section 8.

## **2. Satellite data and model experiments**

### **2.1. OMI Satellite Data.**

We include OMI/MLS tropospheric column ozone (TRCO) for October 2004 – December 2019 and OMI NO<sub>2</sub>, HCHO data for latitude range 60° S – 60° N (Ziemke et al., 2006; De Smedt et al., 2021; Lamsal et al., 2021). OMI/MLS TRCO is determined by subtracting MLS stratospheric column ozone (SCO) from OMI total column ozone each day at each grid point. Tropopause pressure used to determine the SCO invoked the World Meteorological Organization (WMO) 2 K km<sup>-1</sup> lapse-rate definition from the NCEP reanalysis. The MLS data used to obtain SCO were derived from the MLS v4.2 ozone profiles. We estimate 1σ precision for the OMI/MLS monthly mean gridded TRCO product to be about 1.3 DU. Adjustments for drift calibration and other issues (e.g., OMI row anomaly) affecting OMI/MLS TRCO are discussed by Ziemke et al. (2019) and Gaudel et al. (2024).

We used OMI monthly mean Level 3 (L3) data for NO<sub>2</sub> and HCHO (<https://doi.org/10.18758/h2v1uo6x>) that were produced in the context of the ESA CCI+ precursors for aerosols and ozone project (De Smedt et al., 2021; Anglou et al., 2024). The datasets consist of the monthly mean tropospheric column densities for NO<sub>2</sub> and HCHO (based on the QA4ECV NO<sub>2</sub> and HCHO dataset) as measured by OMI from October 2004 to March 2019, and include minimum spatial and temporal coverage thresholds (De Smedt et al., 2018). OMI has an overpass time of 13.30 local time and the retrieved column densities concern clear-sky or partially cloudy conditions.

## 156 2.2 IASI-SOFRID

157 The Software for a Fast Retrieval of Infrared Atmospheric Sounding Interferometer (IASI) data  
 158 (SOFRID) retrieves global ozone profiles from IASI radiances (Barret et al., 2011, 2021). It is  
 159 based on the RTTOV (Radiative Transfer for TOVS) operational radiative transfer model  
 160 jointly developed by ECMWF, Météo-France, UKMO and KNMI within the NWPSAF  
 161 (Saunders et al., 1999; Matricardi et al., 2004). The RTTOV regression coefficients are based  
 162 on line-by-line computations performed using the HITRAN2004 spectroscopic database  
 163 (Rothman et al., 2005), and the land surface emissivity is computed with the RTTOV UW-  
 164 IRemis module (Borbas and Ruston, 2010). The IASI-SOFRID ozone for the study period  
 165 (2008 to 2019) is obtained from METOP-A (2008-2018) and METOP-B (2019).

166 We use the SOFRID version 3.5 data presented and validated in Barret et al. (2021), which  
 167 uses dynamical a priori profiles from an O<sub>3</sub> profile tropopause-based climatology according to  
 168 tropopause height, month, and latitude (Sofieva et al., 2014). The use of such an a priori has  
 169 largely improved the retrievals, especially in the SH where the previous version was biased.  
 170 The retrievals are performed for clear-sky conditions (cloud cover fraction < 20%). IASI-  
 171 SOFRID ozone retrievals provide independent pieces of information in the troposphere, the  
 172 UTLS (300 – 150 hPa), and the stratosphere (150 – 25 hPa) (Barret et al., 2021). SOFRID  
 173 TRCO absolute biases relative to ozonesondes are lower than 8 % with root mean square error  
 174 (RMSE) values lower than 18 % across the six 30° latitude bands (see Barret et al. (2021)).  
 175 Importantly, Barret et al. (2021) have shown that relative to ozonesondes, TRCO from IASI-  
 176 SOFRID display no drifts ( $< 2.1 \text{ \% decade}^{-1}$ ) for latitudes lower than 60°N and in the SH for  
 177 latitudes larger than 30° ( $< 3.7 \text{ \% decade}^{-1}$ ). But significant drifts are observed in the SH tropics  
 178 ( $-5.2 \text{ \% decade}^{-1}$ ) and in the NH at high latitudes ( $12.8 \text{ \% decade}^{-1}$ ).

179

## 180 2.3 IASI+GOME2

181 IASI+GOME2 is a multispectral approach to retrieve the vertical profile of ozone and its  
 182 abundance in several partial columns. It is based on the synergy of IASI and GOME2 spectral  
 183 measurements in the thermal infrared and ultraviolet spectral regions, respectively, which are  
 184 jointly used to improve the sensitivity of the retrieval for the lowest tropospheric ozone (below

3 km above sea level, see Cuesta et al., 2013). Studies over Europe and East Asia have shown particularly good capabilities for capturing near-surface ozone variability compared to surface in situ ozone measurements (Cuesta et al., 2018, 2022; Okamoto et al., 2023). TRCOs from IASI–GOME2 also show good agreement with several datasets of in-situ measurements for a four-year period in the tropics, with almost negligible biases and high correlations (Gaudel et al., 2024). This ozone product provides global coverage for low cloud fraction conditions (below 30%) for 12 km diameter pixels spaced 25 km apart (at nadir). The IASI–GOME2 global dataset is publicly available through the French AERIS data center, with data from 2017 to the present and covers the 90° S – 90° N latitude band. For this study, we use the monthly TRCO data between the surface and the tropopause for 2017 – 2019 for different latitude bands.

## **2.4 TROPOMI**

The TROPOspheric Monitoring Instrument (TROPOMI) is the sole payload on the Copernicus Sentinel–5 Precursor (Sentinel–5P or S5P) satellite, which provides measurements of multiple atmospheric trace species, including NO<sub>2</sub> and HCHO, at high spatial and temporal resolutions (Veefkind et al., 2012). TROPOMI has a daily global coverage with a spatial resolution of 5.5 × 3.5 km<sup>2</sup> at nadir since a long-track pixel size reduction on 6 August 2019. We have used the ESA CCI+ Level–3 gridded 1° x 1° monthly tropospheric column of NO<sub>2</sub> (based on L2 v2.3.1, which applies a retrieval consistent with the most recent TROPOMI L2 version) and HCHO (<https://doi.org/10.18758/2imqez32>) (based on L2 v2.4.1, collection 3) data from May 2018 to December 2019 for our study (De Smedt et al., 2021; Glissenaar et al., 2024). This dataset was created using the same methods as the ESA CCI+ OMI Level–3 datasets.

## **2.5 The ECHAM6-HAMMOZ model experiments**

The ECHAM6.3–HAM2.3–MOZ1.0 aerosol chemistry–climate model (Schultz et al., 2018) used in the present study comprises the general circulation model ECHAM6 (Stevens et al., 2013), the tropospheric chemistry module, MOZ (Stevenson et al., 2006) and the aerosol module, Hamburg Aerosol Model (HAM) (Vignati et al., 2004). The gas phase chemistry is represented by the Jülich Atmospheric Mechanism (JAM) v002b mechanism (Schultz et al., 2018). This scheme is an update and an extension of terpenes and aromatics oxidation based on the MOZART–4 model (Emmons et al., 2010) chemical scheme. Tropospheric heterogeneous chemistry relevant to ozone is also included (Stadtler et al., 2018). MOZ uses

the same chemical preprocessor as CAM–Chem (Lamarque et al., 2012) and WACCM (Kinnison et al., 2007) to generate a FORTRAN code containing the chemical solver for a specific chemical mechanism. Land surface processes are modelled with JSBACH (Reick et al., 2013). Biogenic VOC emissions are modelled with the MEGAN algorithm (Guenther et al., 2012) which has been coupled to JSBACH (Henrot et al., 2017). The lightning NO<sub>x</sub> emissions are parameterized in the ECHAM6–HAMMOZ as described by Rast et al. (2014). The lightning parameterization is the same in all the simulations. The model simulations were performed for the period 1998 to 2019 using the Atmospheric Chemistry and Climate Model Intercomparison Project (ACCMIP) (Lamarque et al., 2010; Van Vuuren et al., 2011) emission inventory. ACCMIP emission inventory includes emissions from agriculture and waste burning, forest and grassland fires, aircraft, domestic fuel use, energy generation including fossil fuel extraction, industry, ship traffic, solvent use, transportation, and waste management. The model was run at a T63 spectral resolution corresponding to about  $1.8^\circ \times 1.8^\circ$  in the horizontal dimension and 47 vertical hybrid  $\sigma - p$  levels from the surface up to 0.001 hPa. The details of model parameterizations and validation are described by (Fadnavis et al., 2019b, 2019a, 2021b, 2021a, 2022, 2023). We performed five experiments: (1) control (CTL) and four emission sensitivity experiments: (2) doubling anthropogenic emission of NO<sub>x</sub> globally (DoubNO<sub>x</sub>), (3) reducing anthropogenic emissions of NO<sub>x</sub> by 50 % globally (HalfNO<sub>x</sub>), (4) doubling anthropogenic emissions of all VOCs globally (DoubVOC), (5) reducing anthropogenic emissions of all VOCs by 50 % globally (HalfVOC). We performed each experiment from 1998 to 2019 after a spin-up of one year. We used the Representative Concentration Pathway (RCP) 8.5 high emission scenario (Van Vuuren et al., 2011) in all model simulations. In each experiment, the monthly varying AMIP–II sea surface temperature and sea ice representative of the period 1998–2019 were specified as a lower boundary condition. Anthropogenic VOC emissions included in the model are listed in the supplementary table S1.

TRCO is computed from the satellite data and model simulations by averaging O<sub>3</sub> amounts from the surface up to the tropopause. The partial tropospheric column is converted into a mixing ratio assuming a constant ozone mixing ratio in the troposphere. Tropopause considered is as described by the WMO thermal tropopause definition, the lowest level at which the temperature lapse rate decreases to  $2 \text{ K km}^{-1}$  or less (WMO, 1957). The estimated tropopause in the satellite data will show differences since the tropopause is quite variable in space and



time; its location will depend on the employed reanalysis (e.g., Hoffmann and Spang, 2022). The vertical resolution of the satellite and the ECHAM6-HAMMOZ also affect the estimated tropopause. For comparison of the model with satellite datasets, e.g., IASI-SOFRID, OMI/MLS, we use model and satellite data for the same period.

## 2.6 Tropospheric ozone radiative effects

The tropospheric ozone radiative effect (TO3RE) is calculated as in Pope et al. (2024). While the radiative effect calculated in ECHAM6-HAMMOZ also includes impacts of aerosols and dynamical effects, here we isolate TO3RE by using the Rap et al. (2015) tropospheric ozone radiative kernel derived from the SOCRATES offline radiative transfer model (Edwards and Slingo, 1996), including stratospheric temperature adjustments. To calculate the TO3RE, the monthly averaged ECHAM6-HAMMOZ simulated ozone field is multiplied by the offline radiative kernel (at every grid box). It is then summed from surface to the tropopause. The simulated ozone data are mapped onto the spatial resolution of the radiative kernel and then interpolated vertically onto its pressure grid. The equation for each grid box is

$$\text{TO3RE} = \sum_{\text{trop}=\text{surf}} \text{RK}_i \times \text{O}_{3i} \times \text{dp}_i / 100 \quad (1)$$

where TO3RE is the tropospheric ozone radiative effect ( $\text{W m}^{-2}$ ), RK is the radiative kernel ( $\text{W m}^{-2} \text{ppbv}^{-1} 100 \text{ hPa}^{-1}$ ),  $\text{O}_3$  is the simulated ozone grid box value (ppbv), dp is the pressure difference between vertical levels (hPa), and 'i' is the grid box index between the surface pressure level and the tropopause pressure. The tropopause pressure is identified based on the WMO lapse rate tropopause definition. Several past studies have used this approach of using the SOCRATES offline radiative kernel with output from model simulations to derive the TO3RE (Rap et al., 2015; Scott et al., 2018; Rowlinson et al., 2020; Pope et al., 2024).

## 3. Results

### 3.1 Comparison of the simulated seasonal cycle in TRCO, NO<sub>2</sub> and HCHO with satellites retrievals

In this section, we compare the estimated TRCO from the model (CTL) simulation with OMI/MLS (2005 – 2019), IASI-SOFRID (2008 – 2019), and IASI-GOME2 (2017 – 2019) satellite retrievals. We compared simulated TRCO for the same period as individual satellite retrievals. The comparison of monthly mean TRCO is made for 20° latitude bins in Figure 1.

278 In the northern tropics ( $0^{\circ}$  N –  $20^{\circ}$  N) (Fig. 1a), the OMI/MLS data exhibits an annual cycle  
 279 with a peak in April, whereas the model indicates a peak in January. Both datasets show a  
 280 minimum in August. The model underestimates TRCO by 1.8 to 3.9 ppb during March to  
 281 October. In the  $21^{\circ}$  N –  $40^{\circ}$  N and  $41^{\circ}$  N –  $60^{\circ}$  N latitude bands (Fig. 1 b–c), the model shows  
 282 a one-month lead in the peak of the annual cycle compared to OMI/MLS. In the  $21^{\circ}$  N –  $40^{\circ}$   
 283 N band, the model underestimates OMI/MLS TRCO by 2.8 – 6.1 ppb during the summer  
 284 months (May–August), while it overestimates TRCO by 4.1 – 8.3 ppb from October to March.  
 285 The  $41^{\circ}$  N –  $60^{\circ}$  N latitude band exhibits an underestimation in the model by 1.1 – 6.3 ppb  
 286 during June and July, while it overestimates (0.7 – 7.5 ppb) the rest of the year. In the Southern  
 287 Hemisphere (SH), OMI/MLS and the model show a similar pattern in the seasonal cycle. The  
 288 model shows a one-to-two-month lead in the annual cycle. However, the model shows an  
 289 underestimation of TRCO for all months. The model underestimates TRCO by 0.5 to 7.1 ppb  
 290 in the  $0^{\circ}$  –  $20^{\circ}$  S, by 5.1– 15.3 ppb in  $21^{\circ}$  S –  $40^{\circ}$  S, and by 9.2 – 13.8 ppb in the  $41^{\circ}$  S –  $60^{\circ}$  S  
 291 latitude bands. The comparison of TRCO from IASI–SOFRID with the model shows features  
 292 similar to those in the OMI/MLS. In the  $0^{\circ}$  N –  $20^{\circ}$  N latitude band, the model underestimates  
 293 the TRCO by about 3.8 to 7.7 ppb from April to October and in the  $21^{\circ}$  N –  $60^{\circ}$  N latitude band  
 294 by 1.9 – 11.3 ppb in summer (May–August). In the SH, the model shows better agreement with  
 295 IASI–SOFRID than OMI/MLS. During the SH winter (June–August), the model overestimates  
 296 TRCO by 2.8 – 6.5 ppb in the latitude range of  $0^{\circ}$  S –  $40^{\circ}$  S. Conversely, it underestimates  
 297 TRCO by 2.7 – 8.2 ppb in the  $41^{\circ}$  S –  $60^{\circ}$  S throughout the year, which is less compared to  
 298 other satellite datasets. IASI–SOFRID is known to suffer from negative drifts in the SH (Barret  
 299 et al., 2021).

300 Interestingly, the model exhibits a fair agreement with IASI–GOME2 retrieved TRCO during  
 301 the summer months (May–August) in the Northern Hemisphere (NH). During the winter  
 302 months, the estimated TRCO shows a large overestimation of 8.3 – 11.7 ppb in the NH ( $0^{\circ}$  N  
 303 –  $40^{\circ}$  N), while it is underestimated by 8.3 – 11.7 ppb in the  $41^{\circ}$  N –  $60^{\circ}$  N. In the SH, a fairly  
 304 good agreement is observed between the model and IASI–GOME2 TRCO, especially in the  $0^{\circ}$   
 305 S –  $40^{\circ}$  S latitude band. The model overestimates the TRCO by 7.4 – 8.8 ppb in the  $0^{\circ}$  S –  $20^{\circ}$   
 306 S during SH winter and underestimates by 4.7 – 6.7 ppb in the  $21^{\circ}$  S –  $40^{\circ}$  S belt during SH  
 307 summer (December–January–February). An overall underestimation of about 7 – 11.2 ppb in  
 308 TRCO is noted in the  $41^{\circ}$  S –  $60^{\circ}$  S throughout the year. Figure 1 shows that a peak in the  
 309 seasonal cycle in the model is earlier than the three satellite data between  $40^{\circ}$  N and  $40^{\circ}$  S. In

general, the model underestimates TRCO in summer in the NH and overestimates in winter relative to OMI/MLS, and IASI-SOFRID. In the SH, the model underestimates TRCO throughout the year compared to OMI/MLS, IASI-SOFRID, and IASI-GOME2, especially in the  $41^{\circ}\text{N} - 60^{\circ}\text{N}$  band. Although the model-satellite comparison is done for the same period, the differences in sampling between the model and satellite measurements may cause the observed differences. It should be noted that the spatial resolution, coverage, and diurnal sampling time differ among the satellites which also contribute to the observed differences among them.

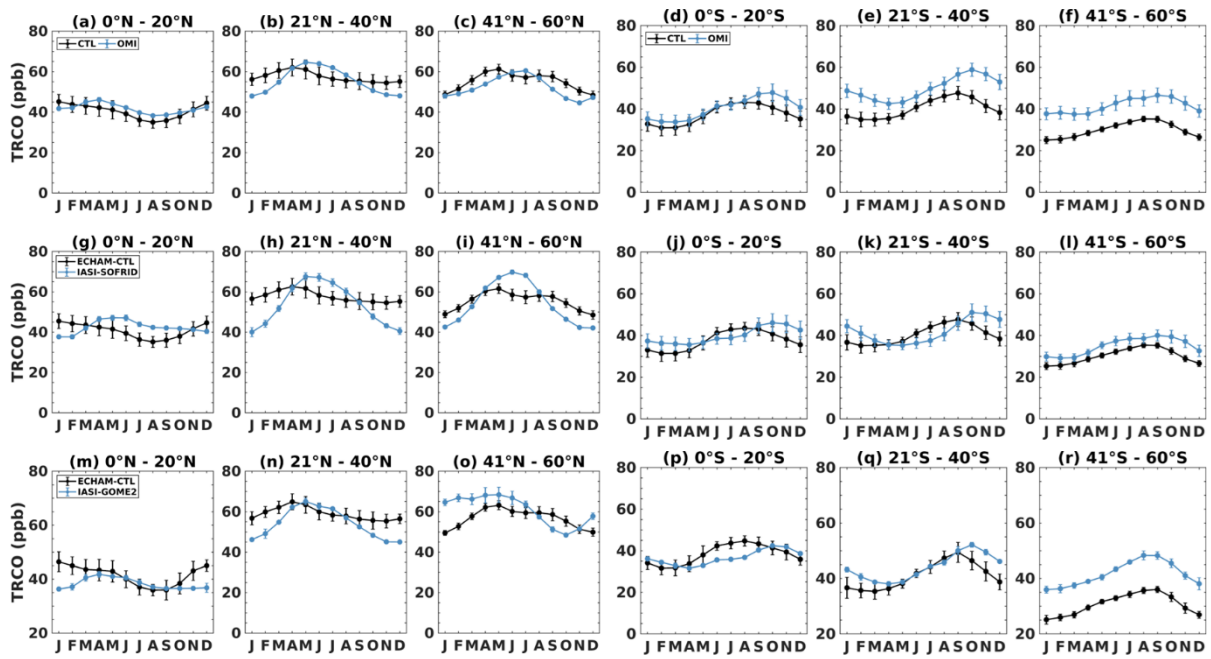


Figure 1. Time series of monthly mean TRCO (ppb) averaged for  $20^{\circ}$  wide latitude bins from (a–f) OMI/MLS (blue) and ECHAM6–HAMMOZ CTL simulations (black) for the time period October 2004 – December 2019. (g–l) same as (a–f) but for IASI–SOFRID (blue) and ECHAM6–HAMMOZ CTL simulations (black) for the period January 2008 – December 2019, and (m–r) same as (a–f) but for IASI–GOME2 (blue) and ECHAM6–HAMMOZ CTL simulations (black) for the time period January 2017 – December 2019. The vertical bars in all the figures represent  $2\sigma$  standard deviation.

To evaluate our model simulations of  $\text{NO}_2$  and  $\text{HCHO}$ , we compare the simulated tropospheric column  $\text{NO}_2$  and  $\text{HCHO}$  with the ESA CCI+ monthly averaged TROPOMI and OMI (Fig. 2). The simulated  $\text{NO}_2$  reproduces the seasonal cycle but shows overestimation in the entire latitude band except  $41^{\circ}\text{S} - 60^{\circ}\text{S}$  in the SH. In the NH, the magnitude of overestimation in the simulated  $\text{NO}_2$  increases with latitude. Simulated  $\text{NO}_2$  is overestimated by 0.15 to 0.35

$\times 10^{15}$  molecules  $\text{cm}^{-2}$  in  $0^\circ \text{N} - 20^\circ \text{N}$ , by 0.3 to  $0.6 \times 10^{15}$  molecules  $\text{cm}^{-2}$  in  $21^\circ \text{N} - 40^\circ \text{N}$ ,  
 and by 0.25 to  $0.9 \times 10^{15}$  molecules  $\text{cm}^{-2}$  in  $41^\circ \text{N} - 60^\circ \text{N}$  latitude bands compared to  
 TROPOMI. Similarly, simulated  $\text{NO}_2$  is overestimated compared to OMI by 0.16 to  $0.35 \times 10^{15}$   
 molecules  $\text{cm}^{-2}$  in  $0^\circ \text{N} - 20^\circ \text{N}$ , by 0.16 to  $0.48 \times 10^{15}$  molecules  $\text{cm}^{-2}$  in  $21^\circ \text{N} - 40^\circ \text{N}$ , and  
 by  $0.18$  to  $0.76 \times 10^{15}$  molecules  $\text{cm}^{-2}$  in  $41^\circ \text{N} - 60^\circ \text{N}$  latitude belt (Fig. 2a–c and 2g–i).  
 Although the model overestimates  $\text{NO}_2$  in the SH, the magnitude of this overestimation is  
 smaller compared to NH. Simulated  $\text{NO}_2$  shows a fairly good agreement from  $21^\circ \text{S}$  to  $60^\circ \text{S}$   
 latitudes in the SH (Fig. 2d–f and 2j–l).

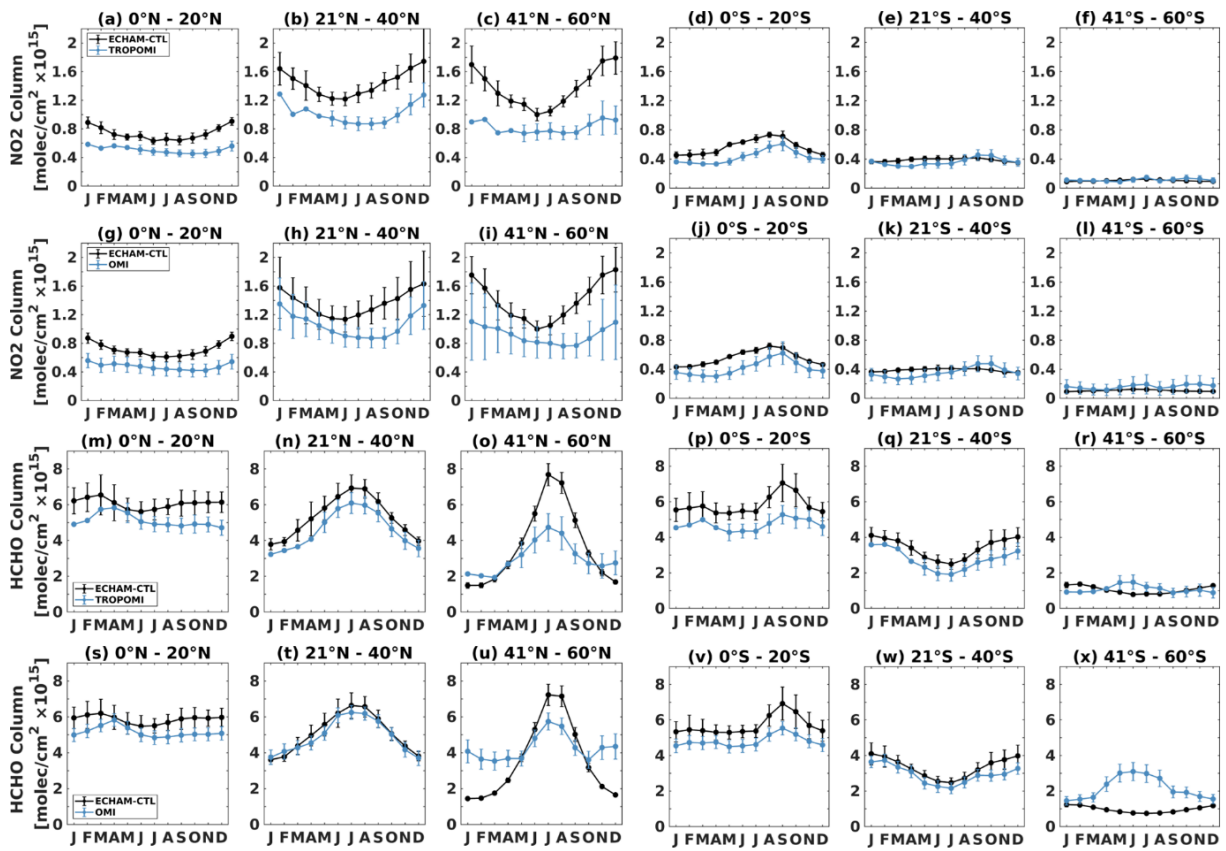


Figure 2. Time series of monthly mean tropospheric column  $\text{NO}_2$  (molecules/ $\text{cm}^2$ ) averaged  
 for  $20^\circ$  wide latitude bins from ECHAM6–HAMMOZ CTL simulations (black) for the time  
 period same as (a–f) TROPOMI from May 2018 to December 2019, and (g–l) OMI from  
 January 2005 to December 2019. (m–x) are the same as that of (a–l) but for HCHO. The vertical  
 bars in the figures represent  $2\sigma$  standard deviation.

While the simulated HCHO successfully reproduces the seasonal cycle in both hemispheres, it shows a large overestimation, particularly in the tropical region (Fig. 2m–x). The overestimation is most pronounced when compared to TROPOMI, especially in the tropics, and to a lesser extent with OMI. The model HCHO aligns reasonably well with both TROPOMI and OMI in the northern and southern mid-latitudes ( $21^{\circ}\text{ N} - 40^{\circ}\text{ N}$  and  $21^{\circ}\text{ S} - 40^{\circ}\text{ S}$ ) with a modest overestimation of  $0.4 - 1.2 \times 10^{15} \text{ molecules cm}^{-2}$  and  $0.3 - 0.5 \times 10^{15} \text{ molecules cm}^{-2}$  respectively in the NH and  $0.4 - 1 \times 10^{15} \text{ molecules cm}^{-2}$  and  $0.5 - 1.4 \times 10^{15} \text{ molecules cm}^{-2}$  respectively in the SH. However, in the  $41^{\circ}\text{ N} - 60^{\circ}\text{ N}$  band, the model overestimates HCHO compared to TROPOMI (OMI) by  $0.6 - 2.9$  ( $0.5 - 1.7$ )  $\times 10^{15} \text{ molecules cm}^{-2}$  during the NH from May to October and underestimates it by  $0.08 - 1.1$  ( $0.01 - 2.7$ )  $\times 10^{15} \text{ molecules cm}^{-2}$  during other months. On the contrary, the model underestimates HCHO in the  $41^{\circ}\text{ S} - 60^{\circ}\text{ S}$  during SH winter. It should be noted that TROPOMI/OMI monthly means are valid for clear-sky situations, whereas the model simulations are all-day all-sky averages. In previous studies (Boersma et al. (2016) and references therein), it was shown that  $\text{NO}_2$  is typically 15 – 20 % lower on clear-sky days than under cloudy situations due to higher photolysis rates, and faster chemical loss of  $\text{NO}_2$ . Further, OMI and TROPOMI cannot sample for snowy scenes, and nighttime. There is significantly lower coverage on the NH during winter and vice versa for SH. These all can likely cause model and satellite differences. For HCHO the effect is smaller because HCHO is both produced and destroyed by OH (see Fig. 4 in Boersma et al. 2016). In addition, diurnal  $\text{NO}_2$  observations from Geostationary Environment Monitoring Spectrometer (GEMS), Edwards et al. (2024) showed that the tropospheric column diurnal  $\text{NO}_2$  variations can be larger than 50 % of the column amount compared to once-a-day TROPOMI observations. Considering these differences, we proceed with the analysis of TRCO trends, ozone photochemical regimes, and ozone radiative effects.

### 3.2. Impacts of emission changes on the spatial distribution of ozone

Figure 3 shows the spatial distribution of the simulated surface (Fig. 3a–e) and TRCO (Fig. 3f–j) concentration from ECHAM CTL simulations and the anomalies obtained from differences in DoubNO<sub>x</sub> - CTL, DoubVOC - CTL, HalfNO<sub>x</sub> - CTL, and HalfVOC - CTL simulations for the period 1998 – 2019. The CTL simulation shows high surface ozone levels (19 – 61.1 ppb) between  $10^{\circ}\text{ N} - 40^{\circ}\text{ N}$  (Fig. 3a). Doubling of NO<sub>x</sub> emission (DoubNO<sub>x</sub>) causes a global mean

enhancement of surface ozone anomalies by 4.1 [-3.8 to 13], [5<sup>th</sup> to 95<sup>th</sup> percentile] ppb. Surface ozone anomalies show an increase of 5 – 20 ppb across most of the globe, excluding highly urbanized regions like the Indo-Gangetic plains (IGP), Southeast China, Northeastern United States (US), and Europe. (Fig. 3b). Over these regions, a large reduction (8 – 20 ppb) in surface ozone anomalies is noticed, indicating ozone titration by NO<sub>x</sub>. While surface ozone anomalies from DoubVOC - CTL simulations show global mean enhancement by 0.9 [0.1 to 2.3] ppb, its magnitude is less than that of the anomalies from DoubNO<sub>x</sub> - CTL (Fig. 3c). The largest increase in surface ozone anomalies for DoubVOC is observed over IGP, Eastern China and the Eastern US (3 – 6 ppb). Interestingly, these are the same regions where a decrease in ozone anomalies is observed in the DoubNO<sub>x</sub> case. The decrease (increase) in ozone anomalies with an increase in NO<sub>x</sub> (VOC) emissions indicates that these regions could be NO<sub>x</sub>-saturated or VOC-limited. Reduction of NO<sub>x</sub> emissions (HalfNO<sub>x</sub>-CTL) simulations show a reduction in surface ozone anomalies (global mean by -2.5 [-7.2 to -0.7] ppb) except over North-Eastern China (Fig. 3d). Earlier, Souri et al. (2017) also reported that eastern Asia has witnessed a rise in surface ozone levels despite NO<sub>x</sub> control strategies, indicating the prevalence of VOC-limited photochemistry over this region (details in section 4 to 6). However, the absence of such an increase over other VOC-limited regions point towards nonlinear ozone chemistry. While HalfVOC - CTL stimulation causes a reduction in surface ozone anomalies (global mean -0.4 [-1.4 to 0.05] ppb), an increase is observed in South America, some parts of the US, Australia, and the Indo-China peninsula (Fig. 3e). This increase could be due to a reduction in the radical destruction of ozone caused by aromatic hydrocarbons in low NO<sub>x</sub> conditions in these regions (Taraborrelli et al., 2021).

Further, we show the impact of emission changes on the TRCO distribution (Fig. 3f–j). The estimated global mean TRCO from the CTL simulation from 1998 to 2019 is 39.4 [23.8 to 56.8] ppb (Fig. 3f). CTL simulations show higher amounts of TRCO (40.9 to 68.8 ppb) in the latitudinal band of 20° N to 40° N. These concentrations are pronounced over South and East Asia, spanning from the Mediterranean region to eastern China (Fig. 3f). TRCO anomalies from DoubNO<sub>x</sub> - CTL show enhancement by 11.7 [6.9 to 19.8] ppb (global mean) (Fig. 3g). Between 20° N – 40° N belt, the TRCO anomalies exceed by 6.1 – 29.3 ppb, particularly over South Asia. Interestingly, in highly urbanized areas such as the IGP, Southeast China, Northeast US, and Europe, there is only a marginal increase in TRCO anomalies (~5 ppb). This



suggests the existence of a distinct ozone photochemical regime in these regions. Further exploration of this aspect will be discussed in sections 4 to 6.

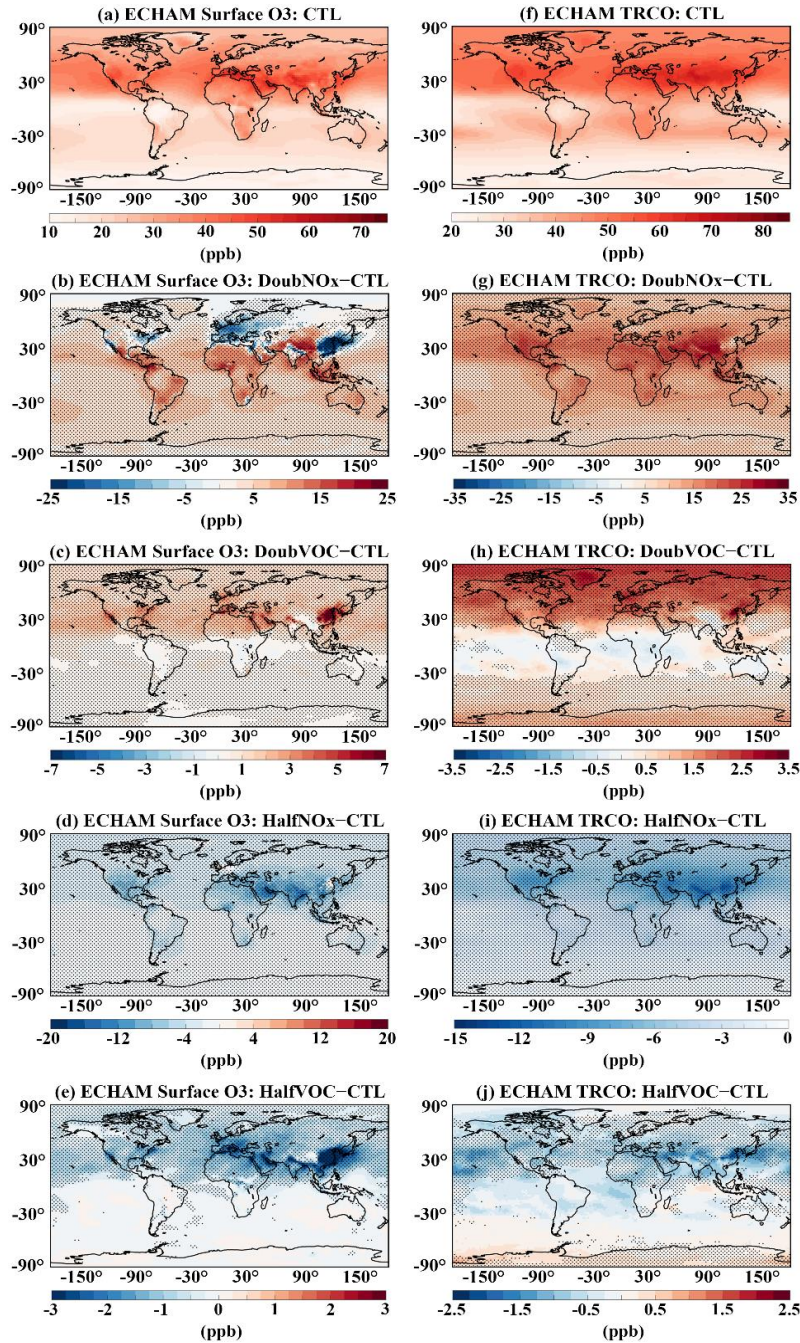


Figure 3. Spatial distribution of surface ozone (ppb) for (a) from CTL simulations, anomalies from (b) DoubNOx - CTL, (c) DoubVOC - CTL, (d) HalfNOx - CTL, and (e) HalfVOC - CTL simulations. (f-j) are the same as that of (a-e) but for TRCO. The stippled regions in the figures indicate anomalies significant at 95% confidence based on the t-test.

The impact of the doubling of VOC emissions (anomalies from DoubVOC - CTL simulations) on TRCO is depicted in Figure 3h. An increase in global mean TRCO by 1 [-0.2 to 2.4] ppb is observed in this emission scenario. It should be noted that TRCO anomalies from DoubVOC - CTL are ten times less than that from DoubNO<sub>x</sub> - CTL (Fig. 3g and 3h). Large values of TRCO anomalies (1.5 – 2) are observed in the high latitudes (north of 60° N) and South and East Asia, with the largest values of more than 2.5 ppb over East China (e.g., Beijing). Interestingly, slight decreases in TRCO are seen in the tropical regions. This is consistent with the recent finding that aromatics, especially benzene, can lead to efficient ozone destruction in tropical UTLS (Rosanka et al., 2021). The TRCO anomalies in response to the reduction of NO<sub>x</sub> emission by 50% (HalfNO<sub>x</sub> - CTL) show negative TRCO anomalies all over the globe (Fig. 3i). The global mean TRCO anomalies are reduced by -3.7 [-7.9 to -1.1] ppb. Large decreases in TRCO anomalies are seen over Arabia, South and East Asian regions (2.6 – 12.8 ppb). The TRCO anomalies from HalfVOC - CTL show an overall decrease in TRCO by -0.27 [-0.97 to -0.4] ppb (Fig. 3j). Further, a small enhancement is noted in the TRCO anomalies (by 0.5 – 1 ppb) in the southern tropics and south polar region, while a decrease of -2.3 to 0.3 ppb is observed in the NH. (Fig. 3j). Figure 3 clearly portrays that the TRCO response to NO<sub>x</sub> emission change is larger than that of VOCs. There is a spatially distinct distribution in TRCO associated with the region-specific ozone photochemical regimes (more discussion on the ozone photochemical regimes will be detailed in sections 4 – 6).

### 3.3. Spatial distribution of trends in ozone

We estimate trends in TRCO from ECHAM CTL simulations (1998–2019) and OMI/MLS satellite retrievals (2005–2019). The simulated trends are compared with satellite retrieves for the period 2005–2019. Since IASI–GOME2 has a short observation period (2017–2019) and IASI–SOFRID has negative drift in the SH, only TRCO from OMI/MLS is considered for trend estimation (Fig. 4). The spatial pattern of trends from OMI/MLS shows fair agreement with model simulations (Fig 4a-b). Quantitatively, the global mean TRCO trend from OMI/MLS is slightly lower than the model (OMI/MLS: 1.43 [-0.5 to 3.2] ppb decade<sup>-1</sup>; ECHAM-CTL: 1.58 [0.3 to 3.3] ppb decade<sup>-1</sup>). Both datasets reveal high trends, ranging from 3–4 ppb decade<sup>-1</sup>, across regions such as South Asia, East Asia, and the West Pacific. OMI/MLS show negative trends over parts of Africa, South America, Australia, and the southeastern Pacific (Fig. 4b), which is not simulated in ECHAM6–HAMMOZ. Although there is fair agreement in spatial



patterns of TRCO trends between OMI/MLS and the model, the minor differences may be due to the model's tendency to underestimate ozone levels and differences in the seasonal cycle. (See Fig. 1).

TRCO trends analyzed from the Total Ozone Mapping Spectrometer (TOMS) indicate a consistent absence of trend over the tropical Pacific Ocean, with notable positive trends ( $4 - 5\%$  decade<sup>-1</sup>) seen in the mid-latitude Pacific regions of both hemispheres (Ziemke et al., 2005). This pattern is consistent across the ECHAM6–HAMMOZ and OMI/MLS data, although their magnitude differs (Fig. 4 a–b). TOMS data also showed trends of  $\sim 2 - 5\%$  decade<sup>-1</sup> across broad regions of the tropical South Atlantic, India, Southeast Asia, Indonesia, and the tropical/subtropical regions of China during 1979 – 2003 (Ziemke et al., 2005; Beig and Singh, 2007) which are also simulated in the model. Further, a large positive trend of  $\sim 2.5$  ppb decade<sup>-1</sup> observed near 50° S in OMI/MLS is not simulated by the model (Fig. 4a–b). The CESM2–WACCAM6 simulation from 1950 to 2014 also shows the largest trend estimate of 0.8 Tg decade<sup>-1</sup> over 20° N – 30° N (Fiore et al., 2022). Large TRCO trends over 20° N – 30° N are also seen in OMI/MLS and the model (Fig.4). Wang et al. (2021) reported TRCO trends varying between 2.55 to 5.53 ppb decade<sup>-1</sup> during 1995–2017 over South and East Asia using IAGOS, ozonesonde observations, and Goddard Earth Observing System–chemistry model (GEOS–Chem). Our model also shows similar increasing trends.

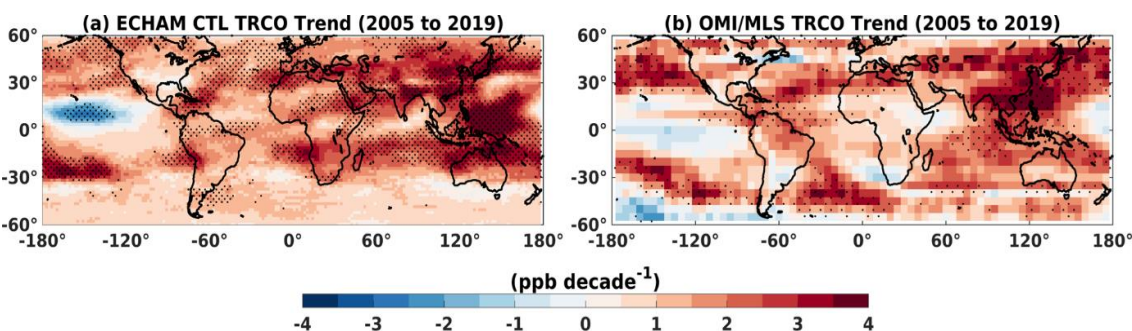


Figure 4. Trend of TRCO (ppb decade<sup>-1</sup>) from (a) ECHAM CTL, and (b) OMI/MLS satellite for the period January 2005 to December 2020. Stippled regions in the figures indicate trends significant at 95% confidence based on the t-test.

Figure 5 shows the spatial distribution of estimated trends in surface ozone and TRCO from CTL simulation for the period 1998 – 2019. Changes (Doubling/halving) in the emission

of NO<sub>x</sub> and VOCs will change ozone trends. Hence, we also analyzed anomalies in ozone from DoubNO<sub>x</sub> - CTL, DoubVOC - CTL, HalfNO<sub>x</sub> - CTL, and HalfVOC - CTL. The surface ozone trend in the CTL simulation shows spatial variation with a pronounced increasing trend over South Asia and the Middle East (3 – 4 ppb decade<sup>-1</sup>) (Fig. 5a). Similar pronounced increase is also seen in the TRCO trend (Fig. 5b). The estimated global mean TRCO trend from CTL is 0.89 [-0.07 to 2.1] ppb decade<sup>-1</sup>. However, the negative trends in surface ozone over Mexico, certain parts of the US, and East China are barely discernible in the TRCO data. This discrepancy may stem from the interplay of mixing and transport processes, stratospheric intrusions, which are crucial when assessing ozone levels across the tropospheric column. The stratospheric ozone intrusions lead enhancement in the tropospheric ozone (Prather and Zhu, 2024).

Figure 5 c–d shows the trend in surface ozone and TRCO estimated from anomalies obtained from DoubNO<sub>x</sub> - CTL simulations. A striking feature is the large negative trend over India and China at the surface (-4.8 to -8 ppb decade<sup>-1</sup>) and TRCO (-2 to -4 ppb decade<sup>-1</sup>). Whereas Europe, the US, some parts of Africa and South America show positive trends at the surface (1.8 to 8 ppb decade<sup>-1</sup>) and TRCO (2 to 4 ppb decade<sup>-1</sup>). The global mean TRCO trend are 1.2 [-0.1 to 2.7] ppb decade<sup>-1</sup>.

When global emissions of VOCs are doubled, the trend in ozone estimated from anomalies (DoubVOC - CTL) shows a decrease (by -0.8 to -1.9 ppb decade<sup>-1</sup>) in surface ozone over Europe, Africa and some parts of the US, while strong positive trend (1.6 to 2 ppb decade<sup>-1</sup>) are seen over India and China (Fig. 5e). TRCO trends show an enhancement over South Asia, Southwest Asia, China, parts of the Indian Ocean, and the western Pacific (0.8 to 1.6 ppb decade<sup>-1</sup>) (Fig. 5f). A global mean TRCO trend for DoubVOC-CTL simulation is 0.5 [-0.03 to 1.04] ppb decade<sup>-1</sup>. The estimated enhancement in global mean TRCO trend for DoubVOC is less than DoubNO<sub>x</sub> simulations. Figures 5 c and e also give indications of the existence of distinct ozone photochemical regimes globally. The increasing (decreasing) trend in surface ozone with an increase in VOC (NO<sub>x</sub>) over India and China indicates that these regions are in a VOC-limited regime, and vice-versa over the US and Europe indicates that these regions are in a NO<sub>x</sub>-limited regime (more discussions on sections 4 to 6).

Figure 5g–h shows the trend in surface and TRCO ozone estimated from anomalies from HalfNO<sub>x</sub> - CTL. The surface ozone trend shows a large negative trend over Europe and South Asia, while a positive trend over the US, China, and Australia (Fig. 5g). Trends in TRCO also show a large negative trend over South Asia (Fig. 5h). Although anthropogenic NO<sub>x</sub> emissions are halved compared to CTL, ozone trends are positive over large region globally. Our investigations reveal that the trend in VOC anomalies from the HalfNO<sub>x</sub>-CTL simulations is positive over the US, India, and Europe, while negative over China. Similarly, the trend in NO<sub>x</sub> anomalies from the HalfNO<sub>x</sub>-CTL simulations is positive over the US and Europe while negative over India and China (Fig. S1a-b). It should be noted that over the US and Europe the positive NO<sub>x</sub> trend estimated from anomalies (HalfNO<sub>x</sub>-CTL) suggests that NO<sub>x</sub> levels in HalfNO<sub>x</sub> are declining more slowly compared to CTL, leading to relatively higher NO<sub>x</sub> concentrations over time. Meanwhile, over India and China, the NO<sub>x</sub> level is weak in HalfNO<sub>x</sub> compared to CTL, leading to a negative trend estimated from NO<sub>x</sub> anomalies (HalfNO<sub>x</sub>-CTL).

It is known that ozone response is non-linear to NO<sub>x</sub> and VOC emission changes and depends on the local photochemical regime. In the US, estimated trends from anomalies are positive in VOC and NO<sub>x</sub> (HALFNOX-CTL). This indicates that relatively more ozone precursors in the HalfNO<sub>x</sub> contribute to the observed positive ozone trend. Over Europe, the strong positive trend estimated from NO<sub>x</sub> anomalies (compared to VOCs) enhances NO<sub>x</sub> titration effects, contributing to the observed negative ozone trend. China, being a VOC–limited regime, experiences reduced NO<sub>x</sub> titration under lower NO<sub>x</sub> conditions, resulting in positive ozone trends. Over India, the positive trend in VOC anomalies with a negative trend in NO<sub>x</sub> anomalies may enhance the radical destruction of ozone caused by aromatic hydrocarbons in low NO<sub>x</sub> conditions (Taraborrelli et al., 2021), resulting in a negative ozone trend. For HalfNO<sub>x</sub> – CTL, the global mean trend is positive 0.47 [-0.76 to 1.3] ppb decade<sup>-1</sup>.

The trend in surface and TRCO ozone estimated from anomalies from HalfVOC – CTL is shown in Figure 5i-j. A large negative trend in surface ozone is noted over IGP and China, while an insignificant positive trend is noted over the US and Europe (Fig. 5i). The TRCO trend are positive over large regions in the world with pronounced high over the mid- and high latitudes although emissions of all anthropogenic VOCs are halved (Fig. 5j). The global mean trend for HalfVOC - CTL is 0.37 [-0.35 to 1.02] ppb decade<sup>-1</sup>. Our analysis shows that the

trend in NO<sub>x</sub> anomalies and VOC anomalies from HalfVOC - CTL is decreasing over both India and China (Fig S1c-d). The negative trend in precursors might have resulted in a negative trend in ozone over these regions. The absence of strong trends in TRCO (Fig. 5 b, d, f, h, j) similar to that at the surface (Fig. 5 a, c, e, g, i) in all the simulations indicates the potential contribution of transport in the troposphere and stratospheric intrusions in TRCO. Ozone injection through stratosphere–troposphere exchange is important source of tropospheric ozone (Prather and Zhu, 2024).

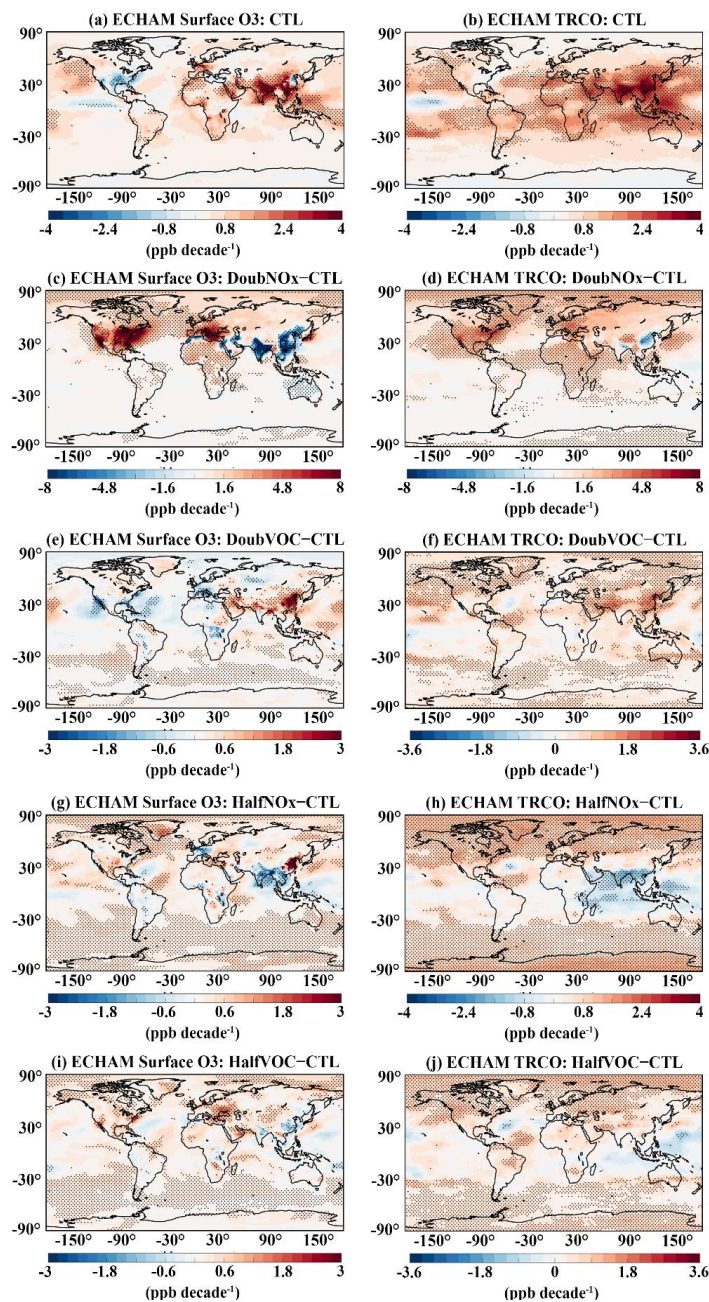


Figure 5. Trend in surface ozone ( $\text{ppb decade}^{-1}$ ) for the period 1998-2019, calculated from (a) CTL, ozone anomalies in (c) DoubNO<sub>x</sub> - CTL, (e) DoubVOC - CTL, (g) HalfNO<sub>x</sub> - CTL, and (i) HalfVOC - CTL simulations. Panels (b, d, f, h, and i) represents the corresponding trend in TRCO. The stippled regions in the figures indicate significance at 95% confidence based on the t-test.

### 3.4. Trends in emission and tropospheric column of NO<sub>2</sub> and HCHO

We show mean emissions of NO<sub>x</sub> (NO+NO<sub>2</sub>) and HCHO over urban/semi-urban regions; US, Brazil, Europe, Africa, India, China, and Australia in Figure 6. High emissions of VOCs and NO<sub>x</sub> in India and China are evident in Figure 6. Furthermore, VOCs emissions are noted to be higher than NO<sub>x</sub> over all the regions. They are higher by a factor of 3.3 in the US, 11.3 in Brazil, 4.8 in Europe, 10.5 in Africa, 10.8 in India, 6.1 in China, and 6.7 in Australia.

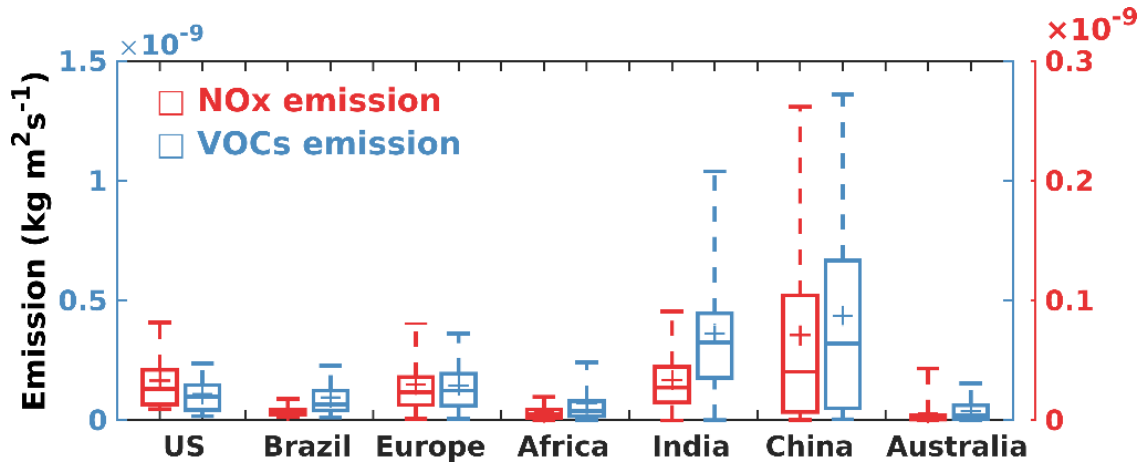


Figure 6. Box and whisker plot illustrating the NO<sub>x</sub> (NO+NO<sub>2</sub>) and VOCs emission over the regions US (85°W – 110°W, 35°N – 44°N), Brazil (34°W – 49°W, 24°S – 3°S), European Union (9°W – 45°E, 35°N – 55°N), Central Africa (14°W – 45°E, 0° – 14°N), India (75°E – 90°E, 8°N – 30°N), China (110°E – 125°E, 30°N – 42°N), and South Australia (134°E – 154°E, 38°S – 28°S) from the ECHAM model. The box represents the 25 and 75 percentiles, and the whisker represents the 5 and 95 percentiles. The plus marker represents the mean, and the horizontal bar represents the 1 and 99 percentiles.

The trends in ozone are partly modulated by the change in the emission of its precursors and partly by meteorology (e.g., Verstraeten et al., 2015). We show trends in emissions and tropospheric column amounts of ozone precursors NO<sub>2</sub> and HCHO from ECHAM CTL and OMI satellite retrievals in Figure 7. NO<sub>2</sub> and HCHO are considered here because column densities of these will be used to identify the ozone photochemical regimes discussed later in

Sections 4–6. Emissions and tropospheric columns of HCHO and NO<sub>2</sub> from ECHAM–CTL show large positive trends over the South and East Asian regions (Fig. 7a–d). These regions show large positive ozone trends in both model and OMI satellite data (see Fig. 4 and 5). Over Europe and the US, the emission trend in both HCHO and NO<sub>2</sub> from the model is negative (Fig. 7a, c). Though a similar negative trend in tropospheric column NO<sub>2</sub> is seen over these regions, a marginal positive trend is noted for HCHO (Fig. 7b, d). The positive trend in column HCHO could be due to secondary production pathways from biogenic emissions or methane oxidation and transport (e.g., Anderson et al., 2017; Alvarado et al., 2020). The positive trend in ozone (Fig. 4a–b and 5a, f) along with a negative trend in NO<sub>2</sub> and HCHO (Fig. 7a–d) over Europe indicates that ozone production over this region has been initially controlled by VOCs (i.e., VOC–limited regime; detailed discussed in section 4). However, a large decreasing trend in NO<sub>2</sub> compared to that of HCHO over this region might have decreased the NO<sub>x</sub> titration effect, resulting in an increase in ozone. On the contrary, a negative trend in surface ozone (Fig. 5a) along with negative trends in NO<sub>2</sub> and HCHO are seen over the US (Fig. 7a–b). The decrease in both NO<sub>2</sub> and HCHO would have resulted in a decreasing trend in surface ozone over this region. This also indicates that the US might have been in a NO<sub>x</sub>–sensitive regime before and the large negative trend in NO<sub>2</sub> might have resulted in the decreasing trend in ozone (discussed further in section 4–6).

Further we compared the simulated trends in column HCHO and NO<sub>2</sub> with the OMI retrievals for the period 2005–2019 (Fig. 7e–h). OMI shows a positive trend in tropospheric column HCHO over South Asia ( $1 - 1.5 \times 10^{15}$  molecules cm<sup>-2</sup> decade<sup>-1</sup>), parts of western China ( $0.75 - 1.25 \times 10^{15}$  molecules cm<sup>-2</sup> decade<sup>-1</sup>), the Iranian Plateau ( $0.5 - 1 \times 10^{15}$  molecules cm<sup>-2</sup> decade<sup>-1</sup>), the Amazon ( $1 - 1.5 \times 10^{15}$  molecules cm<sup>-2</sup> decade<sup>-1</sup>), North America ( $0.5 - 1.5 \times 10^{15}$  molecules cm<sup>-2</sup> decade<sup>-1</sup>), Europe ( $0.5 - 1 \times 10^{15}$  molecules cm<sup>-2</sup> decade<sup>-1</sup>), and central Africa ( $1 - 1.5 \times 10^{15}$  molecules cm<sup>-2</sup> decade<sup>-1</sup>). The model simulated trends show reasonable agreement with OMI, except for western areas in central Africa, north Africa, southwest and southeast China, and some parts of Australia. Over these regions OMI indicates a negative trend, while the model suggests a marginal positive trend. OMI and ECHAM CTL show a good agreement in the tropospheric column NO<sub>2</sub> trend. Both datasets show negative trends over the eastern US and Europe, and positive trends over the Middle East, and South Asia. However, differences are seen in eastern China and central Africa, where OMI indicates a negative trend,



while the model shows a strong positive trend. The differences between simulated and OMI HCHO and NO<sub>2</sub> column trends may be due to sampling time and differences in seasonal cycle. Figures 4, 5, and 7 clearly indicate the impact of ozone precursors on the spatial distribution of ozone trends. This warrants a detailed discussion on the spatial distribution of ozone precursors and their impact on ozone production-sensitive regimes, which will be presented in the next section.

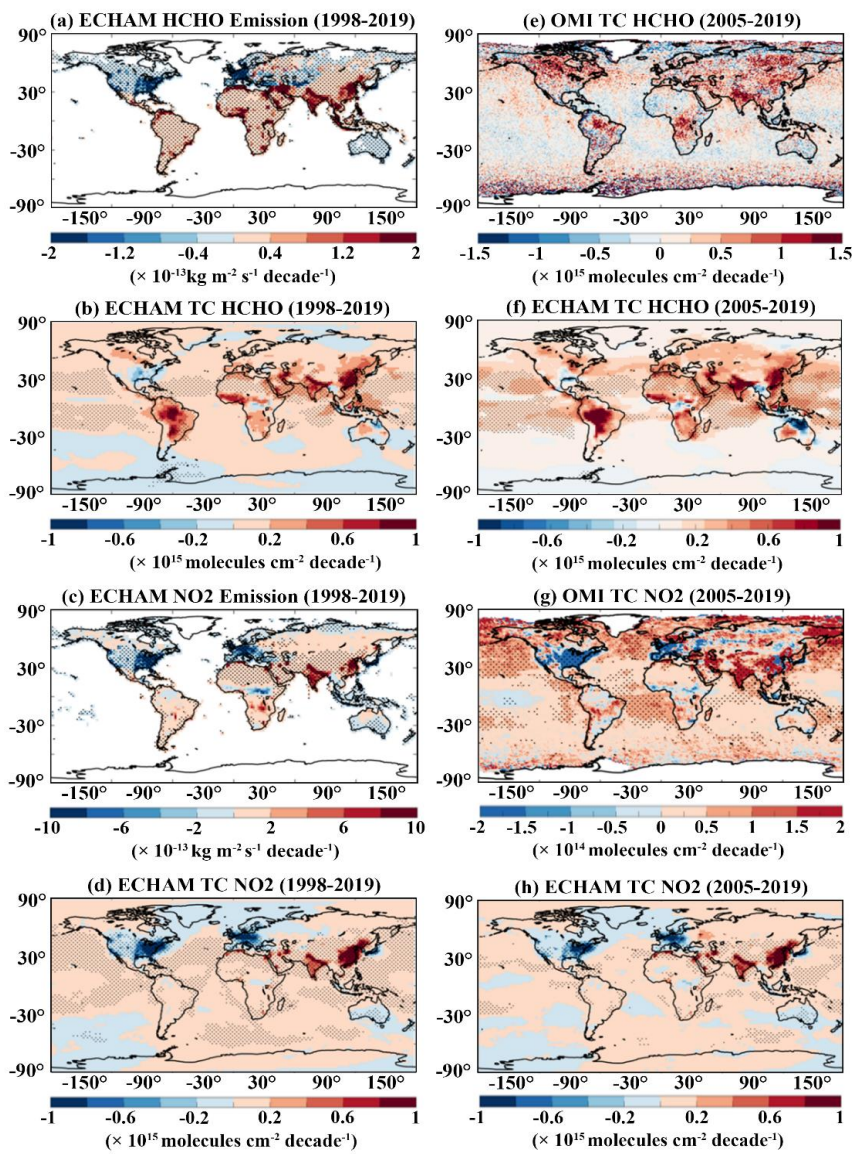


Figure 7. Trend in anthropogenic emission ( $\text{kg m}^{-2} \text{s}^{-1} \text{decade}^{-1}$ ) from ECHAM CTL simulation for the period 1998–2019 for (a–b) HCHO and NO<sub>2</sub> respectively. Trends in tropospheric column (TC) ( $\text{molecules cm}^{-2} \text{decade}^{-1}$ ) for (c–d) HCHO and NO<sub>2</sub> respectively. Trend in tropospheric column of HCHO from (e) OMI, and (f) ECHAM–CTL simulations for the period 2005–2019. (g–h) are the same as that of (e–f) but for tropospheric column NO<sub>2</sub>. The stippled regions in the figures indicate significance at 95% confidence based on the t-test.

#### 4. Influence of NO<sub>x</sub> and VOCs emissions on Formaldehyde to Nitrogen dioxide Ratio

In this section, we diagnosed the spatial distribution of tropospheric ozone production sensitivity regimes (NO<sub>x</sub>-limited/VOC-limited) associated with simulations of emission changes by using formaldehyde to nitrogen dioxide ratio (FNR). We estimate the FNR thresholds from ECHAM6–HAMMOZ model simulations adhering to the methodology outlined by Jin et al. (2017). The procedure to obtain FNR threshold from monthly mean data involves two steps: (1) obtaining the ozone response from emission sensitivity simulations (here, HalfNO<sub>x</sub> and HalfVOC simulations) by considering only the polluted cells over the study region and plotting it as a function of FNR (Fig. 8a), (2) calculating cumulative probability from this data for the conditions  $d[O_3]/dE_{NO_x} < 0$  (VOC limited) and  $d[O_3]/dE_{NO_x} > d[O_3]/dE_{VOC} > 0$  (NO<sub>x</sub>-limited) (Fig. 8b), where  $d[O_3]/dE$  represents the change in ozone corresponding to a change in emission of either NO<sub>x</sub> or VOCs. This approach is applied to estimate FNR thresholds to distinctly delineate the ozone photochemical regimes as NO<sub>x</sub> or VOC-limited over major urban and semi-urban regions. The regions considered for estimating the FNR are shown in Figure 9.

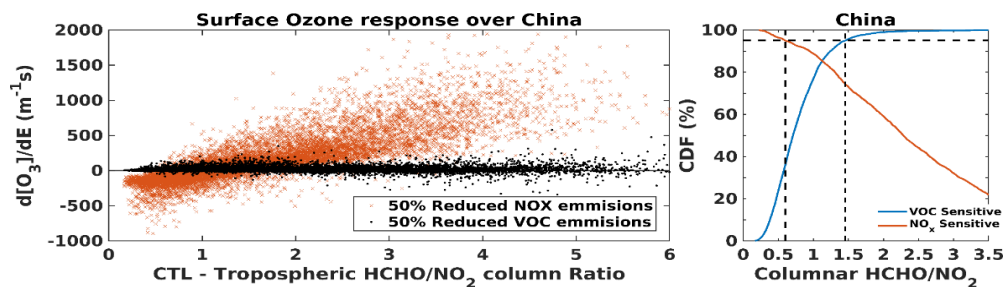


Figure 8. (a) Typical example of a normalized surface ozone sensitivity to a 50% reduction in global NO<sub>x</sub> (HalfNO<sub>x</sub>) and VOC (HalfVOC) emissions versus tropospheric column HCHO/NO<sub>2</sub> ratio derived from ECHAM6–HAMMOZ model simulation over China for the period 1998 – 2019, (b) Cumulative probability (CP) of VOC-sensitive ( $d[O_3]/dE_{NO_x} < 0$ ) and NO<sub>x</sub>-sensitive ( $d[O_3]/dE_{NO_x} > d[O_3]/dE_{VOC} > 0$ ) conditions, as a function of tropospheric column HCHO/NO<sub>2</sub> as simulated by the ECHAM6–HAMMOZ model. The horizontal dashed line represents the 95% CP, and the vertical dashed lines represent the HCHO/NO<sub>2</sub> ratio corresponding to 95% CP for both the VOC-sensitive and NO<sub>x</sub>-sensitive curves demarcating the VOC-sensitive, NO<sub>x</sub>-sensitive, and transition regimes.

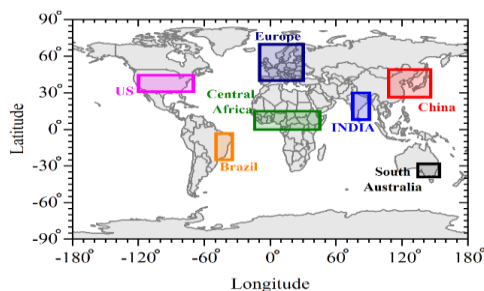




Figure 9. The rectangular box marks indicate the regions considered for estimating the HCHO/NO<sub>2</sub> ratio (FNR).

Further, we compared the model-estimated FNR with the OMI-derived FNR for the period 2005 – 2019. Figure 10 illustrates the comparison of FNR estimated from ECHAM6–HAMMOZ CTL simulations with OMI. The spatial map of FNR shows fairly good agreement between OMI and the model. Over the urbanized regions (e.g., South Asia, Europe, the US, and China) both the model and OMI show FNR < 4. In contrast, regions like North Canada, South America, central Africa, Australia, and Siberia exhibit high FNR values >9. There is good agreement between the model simulations and OMI, however, some minor differences are seen between the model and OMI FNR over the west coast of South America, South Africa, the Tibetan Plateau, and western Australia.

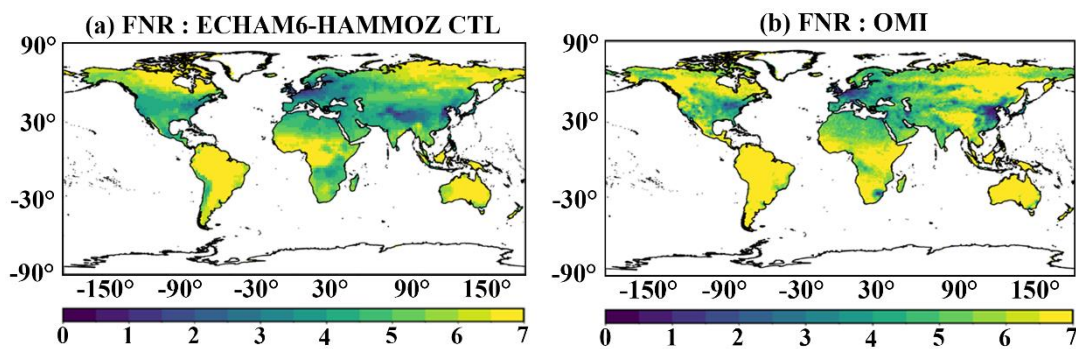


Figure 10. Spatial distribution of mean tropospheric column HCHO/NO<sub>2</sub> (FNR) obtained from ECHAM6–HAMMOZ CTL simulations (2005 – 2019) and OMI (2005 – 2019).

These differences could be due to the underestimation of HCHO in the model over these regions. Considering the fair performance of the model in comparison with OMI, we further analyzed the influence of changes in NO<sub>x</sub> and VOC emissions on the FNR from the model simulations, which are discussed in the subsequent sections.

Since the emission of HCHO and NO<sub>2</sub> varies with the seasons across the globe (e.g., De Smedt et al., 2015; Wang et al., 2017; Surl et al., 2018; Kumar et al., 2020; Goldberg et al., 2021; Guan et al., 2021), understanding the seasonal changes in FNR is crucial for comprehending shifts in ozone photochemical regimes. In this regard, we extracted the seasonal changes in

transition limits for the major urban and semi-urban regions shown in Figure 9 and summarized in Table 3. Figure 11 illustrates the seasonal variation of estimated FNR from both OMI data and model simulations across these key urban regions. In general, all regions exhibit distinct seasonal variations in transition limits (Table 3). Previously reported transition limits over the US (2 – 5: Johnson et al., 2024; 1.1 – 4: Schroeder et al., 2017) and China 0.6 – 1.5/1.25 – 2.39 (Chen et al., 2023) during the summer season are also compared with our model estimates. The estimated FNR values from the ECHAM6–HAMOZ simulations show fair agreement over both locations (0.4 – 4.6 in the US and 0.58 – 2.56 in China) with some minor differences. These minor discrepancies in the estimated FNR could be due to differences in the chosen location, time period and dataset used. Chen et al. (2023) have also reported that the transition limits depend on the region considered for the analysis.

Based on the threshold values depicted in Table 3 and the mean FNR in Figure 11, the seasonal change in ozone photochemical regimes over the key regions associated with the different emission scenarios are assessed. In the CTL simulation (Fig. 11e – h), the US, Europe, and China are found to be in the transition regime, while all other regions are NO<sub>x</sub>–limited during winter. In spring, every region except India remains NO<sub>x</sub>–limited, with India transitioning into the transition regime. During summer and autumn, all regions shift to a NO<sub>x</sub>–limited condition. We further compared the model-estimated regional FNR from the CTL simulation with the OMI-derived FNR shown in Figure 11a – d. The ozone photochemical regimes inferred from both OMI and the model show consistent results except during winter. During winter, the US, Europe and China are NO<sub>x</sub> limited in OMI, while our model shows them in the transition regimes.

Doubling NO<sub>x</sub> (DoubNO<sub>x</sub>) leads to a shift to a VOC–limited regime in all regions except Africa and Australia during winter, spring, and autumn (Fig 11i – l). The relatively high VOC contributions in Africa and Australia likely keep these regions in the transition regime. During summer, the US, Europe, Africa and Australia transform to the transition regimes, while all other regions remain VOC–limited. In both the DoubVOC and HalfNO<sub>x</sub> scenarios (Fig 11m – t), ozone photochemical regimes show no seasonality. All regions consistently exhibit a NO<sub>x</sub>–limited regime throughout all seasons. In the HalfVOC simulation (Figure 11u – x), the US, Europe, and China are in transition regimes, while all other regions become NO<sub>x</sub>–limited

during winter. India remains in a transition regime during all other seasons, whereas other regions consistently exhibit NO<sub>x</sub>–limited conditions. Figure 11 also depicts that DoubNO<sub>x</sub> and HalfNO<sub>x</sub> simulations greatly impact the shift in ozone photochemical regimes compared with DoubVOC and HalfVOC simulations. This indicates that ozone photochemistry is highly sensitive to changes in NO<sub>x</sub> emissions globally.

Table 3. Seasonal mean estimated values of the tropospheric HCHO/NO<sub>2</sub> columns threshold ratios from ECHAM6–HAMMOZ model control simulation to identify the NO<sub>x</sub> and VOC sensitive regimes across regions mentioned in Figure 9. The FNR less than the lower limit indicates VOC–limited, and that higher than the upper limit indicates NO<sub>x</sub>–limited regimes.

Sr. No.	Regions	Transition limits of FNR							
		DJF		MAM		JJA		SON	
1	US	0.48	1.04	0.49	1.15	0.49	4.69	0.45	1.39
2	Brazil	2.93	7.79	2.93	6.66	2.93	6.02	3.12	8.44
3	European Union	0.33	1.13	0.33	1.17	0.33	3.32	0.3	1.45
4	Central Africa	2.95	7.26	2.92	5.66	2.93	6.56	3.14	7.06
5	India	2.23	3.91	2.22	9.19	2.22	5.76	2.27	5.29
6	China	0.56	1.85	0.57	1.86	0.58	2.56	1.14	2.01
7	South Australia	1.1	5.54	1.09	2.3	1.09	1.82	1.12	3.93

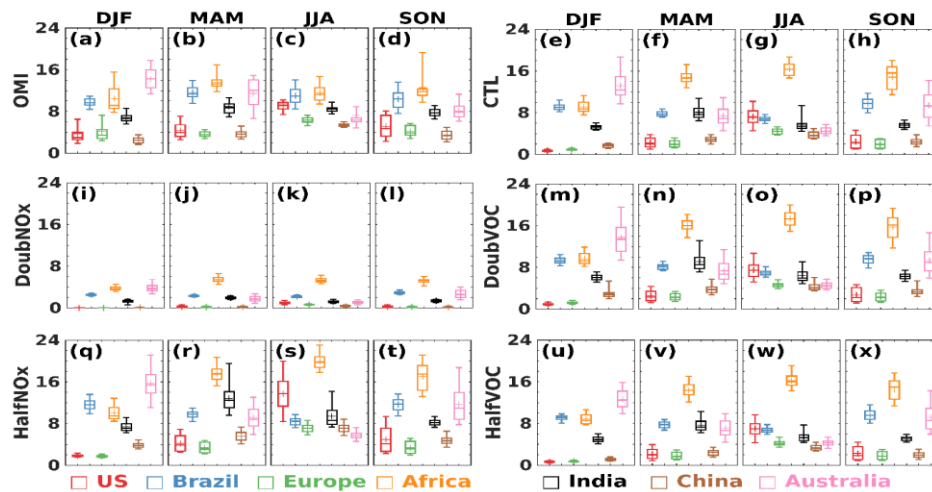


Figure 11. Box and whisker plot illustrating the long-term seasonal average FNR over the regions depicted in Fig.7 from (a-d) OMI observations, and model (e-h) CTL, (i-l) DoubNO<sub>x</sub>, (m-p) DoubVOC, (q-t) HalfNO<sub>x</sub>, and (u-x) HalfVOC simulations. Box represents 25 and 75 percentile and whisker represents 5 and 95 percentiles. The plus marker represents the mean, and the horizontal bar represents the 1 and 99 percentiles.

## **5. Influence of NO<sub>x</sub> and VOCs emissions on trends of Formaldehyde to Nitrogen dioxide Ratio**

Trend analysis is carried out on FNR to understand the temporal evolution of ozone photochemical regimes associated with different emission scenarios. Figure 12 illustrates trends of FNR during the period 1998 – 2019 from CTL, DoubNO<sub>x</sub>, DoubVOC, HalfNO<sub>x</sub>, and HalfVOC simulations. In CTL simulation, decreasing (negative) trends in FNR are seen over the Asian region ( $-0.4$  to  $-1.2$  decade<sup>-1</sup>) and Australia ( $-0.8$  to  $-1.6$  decade<sup>-1</sup>), and an increasing (positive) trend in Europe ( $0.2$  decade<sup>-1</sup>) and the US ( $0.8$  –  $1.4$  decade<sup>-1</sup>) (Fig. 12a). These observed trends in FNR are mainly driven by the region-specific trends in HCHO and NO<sub>2</sub> (Fig. 7). Figure 7 shows a higher positive trend in NO<sub>2</sub> than in HCHO in the Asia region, causing an overall decreasing trend in FNR, indicating a tendency towards VOC-limited regimes. Whereas, over the US and Europe, there is a higher negative trend in NO<sub>2</sub> than HCHO, causing a positive trend in FNR, indicating a tendency towards a NO<sub>x</sub>-limited regime. A recent study by Elshorbany et al. (2024) also reported a significant positive trend over Europe and the US and a negative trend over Asia using the OMI-based tropospheric column HCHO/NO<sub>2</sub> ratio. Further, long-term column measurements of HCHO and NO<sub>2</sub> from OMI over India and China have revealed an increasing trend in NO<sub>2</sub> compared to that of HCHO, causing a decreasing trend in FNR over these regions (Jin and Holloway, 2015; Mahajan et al., 2015).

DoubNO<sub>x</sub> simulation (Fig. 12b) shows a similar spatial trend pattern to that of CTL simulation (Fig. 12a). However, the magnitude of this trend is less than that of the CTL. For example, a weak positive trend is noted in the US and Europe ( $0.2$  –  $0.4$  decade<sup>-1</sup>), while trends over India, and China are less negative ( $-0.2$  to  $-0.4$  decade<sup>-1</sup>) in DoubNO<sub>x</sub> than CTL. (Fig. 12b). On the contrary, the magnitude of the positive trend over Canada and the negative trend over central Africa increased in DoubNO<sub>x</sub> emission, while the negative trend over Australia became nominal and insignificant. This indicates that Canada and central Africa have a tendency to become NO<sub>x</sub>-limited and VOC-limited respectively.

In DoubVOC simulations, trends are marginally increasing over the US, Canada, and Europe compared to the CTL (Fig. 12a and 12c). A notable change is observed over the Middle East and Amazon, where trends become more negative and positive respectively compared to CTL. The negative trends over Australia in the CTL become nominal and insignificant in the DoubVOC simulation. In HalfNO<sub>x</sub> simulations (Fig. 12d), the positive trends are higher over

the US, Europe and Amazon, while negative trends prevail over India, China and northeast Australia. Meanwhile, in HalfVOC simulation, marginal changes are noted globally compared to CTL. The most pronounced change in the FNR trend is observed over West Australia, where the negative trend in CTL becomes positive in HalfVOC (Fig. 12e). Figure 12f clearly shows that the trend in FNR is always negative over India and China for all the simulations, indicating that these regions have a tendency to become VOC-limited, while the positive trends over Europe and US show a tendency to become more NO<sub>x</sub>-limited. Further, from Figures 5, 11 and 12, we can infer that the relation between trends in FNR and ozone exhibits a nonlinearity. For example, even though FNR shows a negative trend over India and China for all the simulations, the TRCO trend depends on the specific emission scenario.

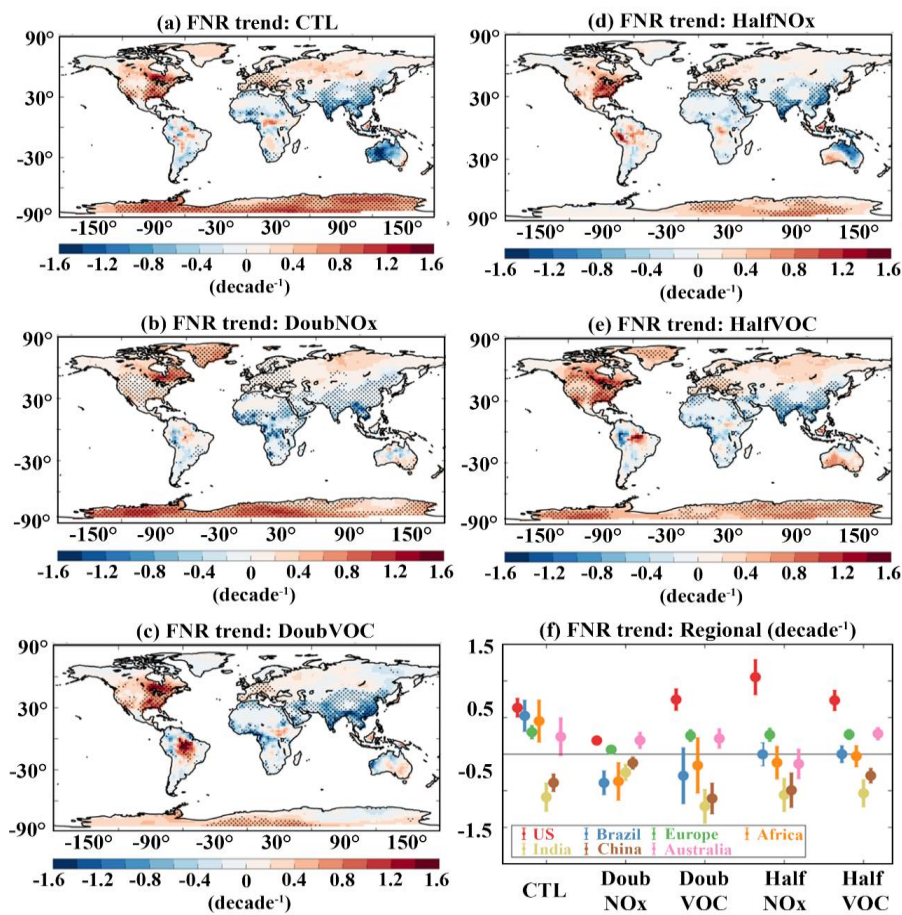


Figure 12. Trends in the tropospheric column HCHO/NO<sub>2</sub> ratio during 1998 – 2019 from ECHAM6–HAMMOZ simulations for (a) for CTL, (b) DoubNO<sub>x</sub>, (c) DoubVOC, (d) HalfNO<sub>x</sub>, (e) HalfVOC simulations. The stippled region indicates the trend significant at 95% confidence based on the t-test. (f) scatter plot illustrating the long-term trend and standard deviation over the regions depicted in Fig.9.

## 6. Tropospheric ozone radiative effects

The impact of emission changes on the tropospheric ozone radiative effect (TO3RE) is estimated using the ECHAM6 model output and a radiative kernel method (see data and model experiments). The estimated TO3RE for different model simulations are shown in Figure 13. In the CTL simulations (Fig. 13a), the estimated global mean area-weighted average TO3RE for the period 1998 to 2019 is  $1.21 [1.1 \text{ to } 1.3] \text{ W m}^{-2}$ . High TO3RE is noted over North Africa and the Middle East region in NH ( $\sim 2.2 \text{ W m}^{-2}$ ), while in SH, it is over Australia and South Africa ( $\sim 1.2 \text{ W m}^{-2}$ ). TO3RE estimates from TES measurements (2005 – 2009) also show a peak of  $1.0 \text{ W m}^{-2}$  in northern Africa, the Mediterranean, and the Middle East in June–July–August (Bowman et al. 2013). Recently, Pope et al. (2024) reported TO3RE estimates from IASI–SOFID, IASI–FORLI, and IASI–IMS for the period 2008 – 2017. The values reported by Pope et al. (2024) are comparable with our CTL simulation (e.g. IASI–FORLI:  $1.23 \text{ W m}^{-2}$ , IASI–SOFID:  $1.21 \text{ W m}^{-2}$ , IASI–IMS:  $1.21 \text{ W m}^{-2}$ , ECHAM6:  $1.22 \text{ W m}^{-2}$ ).

The anomalies of TO3RE from DoubNOx-CTL simulations are shown in Figure 13b. Doubling of NOx emission causes an enhancement in TO3RE by  $0.36 [0.23 \text{ to } 0.5] \text{ W m}^{-2}$  compared to the CTL simulation. It shows a peak over the Middle East and adjacent North Africa ( $0.7 \text{ W m}^{-2}$ ). A similar peak over this region is also seen in the CTL simulation. Doubling of VOC emissions causes a marginal decrease in global mean TO3RE by  $-0.005 [-0.05 \text{ to } 0.04] \text{ W m}^{-2}$ . TRCO enhancement for doubling NOx is also higher than doubling VOC (see Fig.3). DoubVOC-CTL simulations (Fig. 13 c) show a peak over the Arctic ( $0.02 \text{ W m}^{-2}$ ). The TO3RE anomalies are negative between  $30^\circ \text{ N} - 30^\circ \text{ S}$ . These negative anomalies in TO3RE between  $30^\circ \text{ S} - 30^\circ \text{ N}$  (Fig. 13c) can be attributed to negative anomalies of TRCO (Fig. 3h). The reduction of NOx emission by 50% reduced global mean TO3RE by  $-0.12 [-0.2 \text{ to } -0.05] \text{ W m}^{-2}$  than CTL. The anomalies in TO3RE from HalfNOx-CTL simulations (Fig. 13d) show negative anomalies all over the globe, with a strong decrease over the Middle East and adjacent North Africa ( $-0.25 \text{ W m}^{-2}$ ). Figures 13b and 13d show that the effect of enhancement/reduction of NOx emission is high over the Middle East and adjacent North Africa. The reduction of VOC emission by 50% reduced global mean TO3RE by  $-0.03 [-0.07 \text{ to } 0.02] \text{ W m}^{-2}$  than CTL simulations (Fig. 13e). HalfVOC - CTL simulations show negative



anomalies of TO3RE between 40° S – 40° N and positive 0.015 W m<sup>-2</sup> (low confidence) over mid-high latitudes in NH and SH. From Figure 13, it is interesting to note that the magnitude of TO3RE and its response to emission change is pronounced over the Middle East compared to all other regions. Further, Figure 13f depicts the latitude variation of zonal mean TO3RE for different sensitivity simulations. It is clear from Figure 13f that the TO3RE response to emission change is large at the northern and southern mid-latitudes, around ±30°. Also, Figure 13f clearly indicates that the impacts of NO<sub>x</sub> emission changes are larger than VOCs throughout the latitude band.

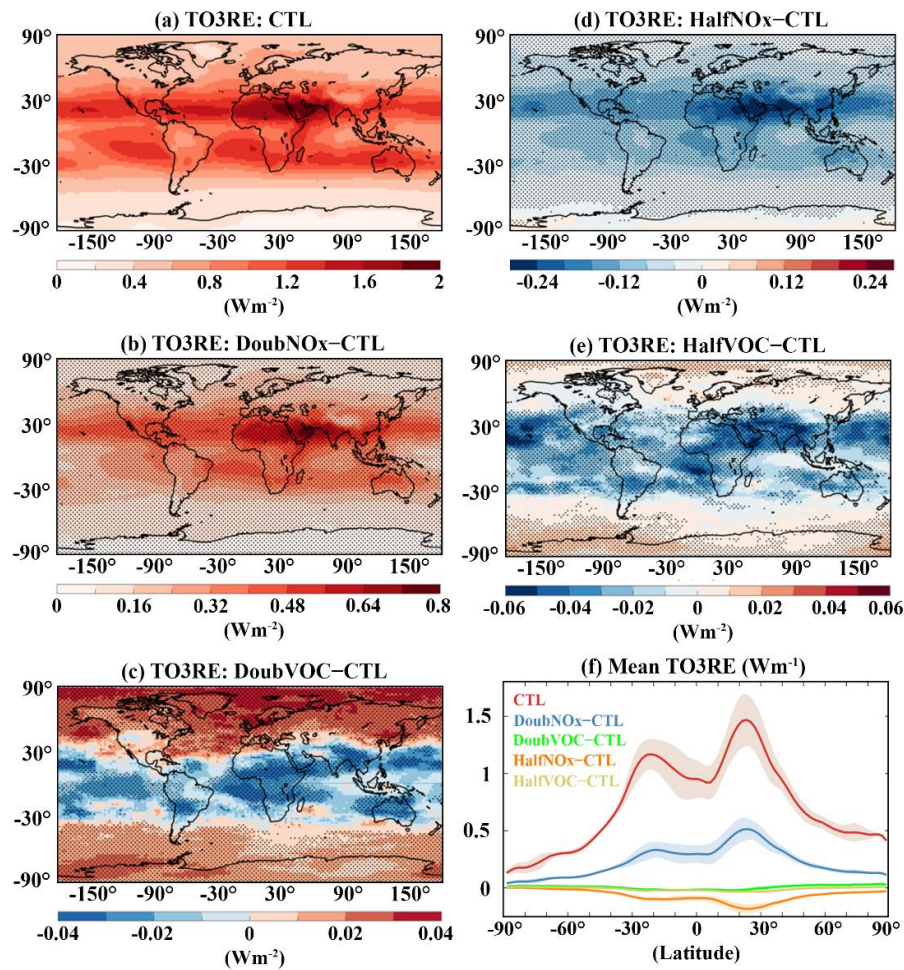


Figure 13. Tropospheric Ozone radiative effects (TO3RE) (W m<sup>-2</sup>) for (a) CTL, and anomalies from (b) DoubNOx - CTL, (c) DoubVOC - CTL, (d) HalfNOx - CTL, (e) HalfVOC - CTL simulations. Stippled regions in Figures (b–e) indicate TO3RE significant at 95 % confidence level based on the t-test, (f) line plot for zonal mean TO3RE (W m<sup>-2</sup>) from CTL, DoubNOx - CTL, DoubVOC - CTL, HalfNOx - CTL, HalfVOC - CTL, shades indicate standard deviation.

## 7 Summary and Conclusions

In this study, we report variation of tropospheric ozone levels, trends, photochemical regimes and radiative effects using the state-of-the-art ECHAM6–HAMMOZ chemistry-climate model simulations from 1998 to 2019. The model simulations are validated against multiple satellite observations. Our analysis shows that

1. The estimated global mean trend in TRCO from CTL simulations for the period 1998 – 2019 is 0.89 [-0.07 to 2.1] ppb decade<sup>-1</sup>. Trend estimates from OMI/MLS (1.43 [-0.5 to 3.2] ppb decade<sup>-1</sup>) for the period January 2005 to December 2019 show good agreement with CTL (1.58 [0.3 to 3.3] ppb decade<sup>-1</sup>) for the same period.
2. TRCO anomalies from DoubNO<sub>x</sub> - CTL simulations show positive trends over Europe, the US, Africa, and South America, with a global mean trend of 1.2 [-0.1 to 2.7] ppb decade<sup>-1</sup>. However, India and China show decreasing TRCO trend -2 to -4 ppb decade<sup>-1</sup>. Surface ozone anomalies over these regions show strong negative trends -4.8 to -8 ppb decade<sup>-1</sup>.
3. Global mean TRCO trend anomalies from DOUBNO<sub>x</sub> - CTL simulation is 1.2 [-0.1 to 2.7] ppb decade<sup>-1</sup>, while for DoubVOC - CTL is 0.5 [-0.03 to 1.04] ppb decade<sup>-1</sup>. Global mean TRCO trend anomalies from HalfNO<sub>x</sub> - CTL is 0.47 [-0.76 to 1.3] ppb decade<sup>-1</sup> and for HalfVOC - CTL is 0.37 [-0.35 to 1.02] ppb decade<sup>-1</sup>.
4. The spatial distribution of TRCO anomalies shows that enhancement is nearly 12 times higher in DoubNO<sub>x</sub> - CTL than in DoubVOC - CTL simulations. The largest increase in surface ozone anomalies from DoubVOC - CTL is observed over Indo-Gangetic Plains, Eastern China and the eastern United States (4 – 6 ppb), where a decrease in surface ozone anomalies is observed in the DoubNO<sub>x</sub> - CTL simulation. This decrease (increase) in ozone with an increase in NO<sub>x</sub> (VOC) indicates that these regions are VOC-limited.
5. The FNR transition thresholds exhibit pronounced seasonal variability. In the CTL simulation, the US, Europe, and China remain in the transition regime during winter, while other regions are predominantly NO<sub>x</sub>-limited. In spring, NO<sub>x</sub>-limited conditions persist across all regions except India. A widespread shift to NO<sub>x</sub>-limited regimes is observed during summer and autumn.



6. The DoubNO<sub>x</sub> simulation indicates a consistent shift toward VOC-limited regimes across most regions, except Africa and Australia, during winter, spring, and autumn. In summer, VOC-limited conditions prevail in most regions, whereas the US, Europe, Africa, and Australia are in a transition regime.
  7. In both the DoubVOC and HalfNO<sub>x</sub> scenarios all regions consistently exhibit a NO<sub>x</sub>-limited regime throughout all seasons. In the HalfVOC simulation the US, Europe, and China are in transition regimes, while all other regions become NO<sub>x</sub>-limited during winter. India remains in a transition regime during all other seasons, whereas other regions consistently exhibit NO<sub>x</sub>-limited conditions.
  8. Comparison of all the emission simulations, DoubNO<sub>x</sub> and HalfNO<sub>x</sub> simulations influence the shift in tropospheric ozone photochemical regimes compared to DoubVOC and HalfVOC simulations, highlighting the global sensitivity of ozone photochemistry to NO<sub>x</sub> emissions changes.
  9. Trends estimated from modelled FNR are negative over India ( $-0.6 \text{ decade}^{-1}$ ) and China ( $-0.4 \text{ decade}^{-1}$ ) in all the simulations, indicating that these regions have a tendency to become VOC-limited, while the positive trends over Europe ( $0.3 \text{ decade}^{-1}$ ), US ( $0.63 \text{ decade}^{-1}$ ), and Africa ( $0.45 \text{ decade}^{-1}$ ), indicating a tendency to become more NO<sub>x</sub>-limited.
  10. The estimated global mean tropospheric ozone radiative effect (TO3RE) is  $1.21 [1.1 \text{ to } 1.3] \text{ W m}^{-2}$  which is increased by the doubling of NO<sub>x</sub> emissions (DoubNO<sub>x</sub> - CTL) by  $0.36 [0.23 \text{ to } 0.5] \text{ W m}^{-2}$  and VOCs by  $-0.005 [-0.05 \text{ to } 0.04] \text{ W m}^{-2}$  (DoubVOC - CTL). However, halving NO<sub>x</sub> (HalfNO<sub>x</sub> - CTL) emissions shows a reduction in the global mean TO3RE by  $-0.12 [-0.2 \text{ to } -0.05] \text{ W m}^{-2}$  and VOC (HalfVOC - CTL) by  $-0.03 [-0.07 \text{ to } 0.02] \text{ W m}^{-2}$ .
  11. We show that anthropogenic NO<sub>x</sub> emissions have a higher impact on tropospheric ozone levels, trends, and radiative effects than VOC emissions globally.
- Our study highlights the dominant role of anthropogenic NO<sub>x</sub> emissions in shaping tropospheric ozone trends, photochemical regimes, and radiative forcing over the past two decades. Sensitivity experiments reveal that NO<sub>x</sub> emission changes have a significantly larger impact on ozone levels and radiative forcing than VOCs, with regions transitioning from VOC-limited to NO<sub>x</sub>-limited regimes as NO<sub>x</sub> reductions continue. With current emission trends, air quality regulations, and industrial growth continuing to evolve, our study reinforces the need for region-specific mitigation strategies to

effectively manage ozone pollution. This study emphasizes the importance of carefully balancing NO<sub>x</sub> and VOC controls to optimize air quality management and climate mitigation efforts. While climate change affects ozone chemistry, its impact over our study period (1998–2019) is minimal, given the relatively small global rate of temperature increase (~0.3–0.4°C) (IPCC AR6). Studies suggest that an ozone climate penalty emerges only after a 2–3°C temperature increase (Zanis et al., 2022), primarily in high-emission regions. Furthermore, rising temperatures increase water vapor, which reduces the ozone lifetime in remote areas. Thus, while climate change will play a growing role in future ozone variability, our findings confirm that anthropogenic emissions remain the dominant driver of recent ozone trends. As mitigation strategies evolve, targeted NO<sub>x</sub> and VOC controls must account for regional photochemical regimes, while future research should explore the potential interactions between climate change, natural VOCs, and ozone formation in a warming world.

**Author's contribution:** SF and YE initiated the manuscript. SF made the model simulations. VS and SC did the analysis of model simulations. Satellite datasets are provided by JZ, BB, EF, IG, ID, MR, IS. All authors contributed to the writing of the manuscript.

**Competing interests:** At least one of the (co-)authors is a member of the editorial board of Atmospheric Chemistry and Physics.

## **Acknowledgements**

S.F. acknowledge the high-performance computing at the Indian Institute of Tropical Meteorology Pune, India for supporting the model simulations. RJP was funded by the UK Natural Environment Research Council (NERC) by providing funding for the National Centre for Earth Observation (NCEO, award reference NE/R016518/1) and funding from the European Space Agency (ESA) Climate Change Initiative (CCI) post-doctoral fellowship scheme (award reference 4000137140).

## **Data availability**

Available from the TOAR FTP server (<ftp://toar@ftpshare.al.noaa.gov>).

## **Code availability**

Available from the corresponding author upon reasonable request.

## **References:**

1063 Alvarado, L. M. A., Richter, A., Vrekoussis, M., Hilboll, A., Kalisz Hedegaard, A. B.,  
 1064 Schneising, O., and Burrows, J. P.: Unexpected long-range transport of glyoxal and  
 1065 formaldehyde observed from the Copernicus Sentinel-5 Precursor satellite during the 2018  
 1066 Canadian wildfires, *Atmos. Chem. Phys.*, 20, 2057-2072, 10.5194/acp-20-2057-2020, 2020.

1067 Anderson, D. C., Nicely, J. M., Wolfe, G. M., Hanisco, T. F., Salawitch, R. J., Canty, T. P.,  
 1068 Dickerson, R. R., Apel, E. C., Baidar, S., Bannan, T. J., Blake, N. J., Chen, D., Dix, B.,  
 1069 Fernandez, R. P., Hall, S. R., Hornbrook, R. S., Gregory Huey, L., Josse, B., Jöckel, P.,  
 1070 Kinnison, D. E., Koenig, T. K., Le Breton, M., Marécal, V., Morgenstern, O., Oman, L. D.,  
 1071 Pan, L. L., Percival, C., Plummer, D., Revell, L. E., Rozanov, E., Saiz-Lopez, A., Stenke, A.,  
 1072 Sudo, K., Tilmes, S., Ullmann, K., Volkamer, R., Weinheimer, A. J., and Zeng, G.:  
 1073 Formaldehyde in the Tropical Western Pacific: Chemical Sources and Sinks, Convective  
 1074 Transport, and Representation in CAM-Chem and the CCM1 Models, *Journal of Geophysical  
 1075 Research: Atmospheres*, 122, 11,201-211,226, <https://doi.org/10.1002/2016JD026121>, 2017.

1076 Anglou, I., Glissenaar, I. A., Boersma, K. F., & Eskes, H. (2024). ESA CCI+ OMI L3 monthly  
 1077 mean NO2 columns [Data set]. Royal Netherlands Meteorological Institute (KNMI).  
 1078 <https://doi.org/10.21944/cci-no2-omi-l3>

1079 Archibald, A. T., Neu, J. L., Elshorbany, Y. F., Cooper, O. R., Young, P. J., Akiyoshi, H., Cox,  
 1080 R. A., Coyle, M., Derwent, R. G., Deushi, M., Finco, A., Frost, G. J., Galbally, I. E., Gerosa,  
 1081 G., Granier, C., Griffiths, P. T., Hossaini, R., Hu, L., Jöckel, P., Josse, B., Lin, M. Y., Mertens,  
 1082 M., Morgenstern, O., Naja, M., Naik, V., Oltmans, S., Plummer, D. A., Revell, L. E., Saiz-  
 1083 Lopez, A., Saxena, P., Shin, Y. M., Shahid, I., Shallcross, D., Tilmes, S., Trickl, T., Wallington,  
 1084 T. J., Wang, T., Worden, H. M., and Zeng, G.: Tropospheric Ozone Assessment Report: A  
 1085 critical review of changes in the tropospheric ozone burden and budget from 1850 to 2100,  
 1086 *Elementa: Science of the Anthropocene*, 8, 10.1525/elementa.2020.034, 2020.

1087 Barret, B., Gouzenes, Y., Le Flochmoen, E., and Ferrant, S.: Retrieval of Metop-A/IASI N2O  
 1088 Profiles and Validation with NDACC FTIR Data, *Atmosphere*, 12, 219, 2021.

1089 Barret, B., Le Flochmoen, E., Sauvage, B., Pavelin, E., Matricardi, M., and Cammas, J. P.: The  
 1090 detection of post-monsoon tropospheric ozone variability over south Asia using IASI data,  
 1091 *Atmos. Chem. Phys.*, 11, 9533-9548, 10.5194/acp-11-9533-2011, 2011.

1092 Beig, G. and Singh, V.: Trends in tropical tropospheric column ozone from satellite data and  
 1093 MOZART model, *Geophysical Research Letters*, 34, <https://doi.org/10.1029/2007GL030460>,  
 1094 2007.

1095 Boersma, K. F., Vinken, G. C. M., and Eskes, H. J.: Representativeness errors in comparing  
 1096 chemistry transport and chemistry climate models with satellite UV–Vis tropospheric column  
 1097 retrievals, *Geosci. Model Dev.*, 9, 875-898, 10.5194/gmd-9-875-2016, 2016.

1098 Borbas, E. and Ruston, B.: The RTTOV UWiremis IR land surface emissivity module, Mission  
 1099 Report EUMETSAT NWPSAF-MO-VS-042. [http://nwpsaf.eu/vs\\_reports/nwpsaf-mo-vs-](http://nwpsaf.eu/vs_reports/nwpsaf-mo-vs-042.pdf)  
 1100 042.pdf, 2010.

1101 Chang, K.-L., Cooper, O. R., Gaudel, A., Allaart, M., Ancellet, G., Clark, H., Godin-  
 1102 Beekmann, S., Leblanc, T., Van Malderen, R., Nédélec, P., Petropavlovskikh, I., Steinbrecht,  
 1103 W., Stübi, R., Tarasick, D. W., and Torres, C.: Impact of the COVID-19 Economic Downturn  
 1104 on Tropospheric Ozone Trends: An Uncertainty Weighted Data Synthesis for Quantifying

1105 Regional Anomalies Above Western North America and Europe, AGU Advances, 3,  
1106 e2021AV000542, <https://doi.org/10.1029/2021AV000542>, 2022.

1107 Chang, K.-L., Cooper, O. R., Rodriguez, G., Iraci, L. T., Yates, E. L., Johnson, M. S., Gaudel,  
1108 A., Jaffe, D. A., Bernays, N., Clark, H., Effertz, P., Leblanc, T., Petropavlovskikh, I., Sauvage,  
1109 B., and Tarasick, D. W.: Diverging Ozone Trends Above Western North America: Boundary  
1110 Layer Decreases Versus Free Tropospheric Increases, *Journal of Geophysical Research:*  
1111 *Atmospheres*, 128, e2022JD038090, <https://doi.org/10.1029/2022JD038090>, 2023.

1112 Chen, Y., Wang, M., Yao, Y., Zeng, C., Zhang, W., Yan, H., Gao, P., Fan, L., and Ye, D.:  
1113 Research on the ozone formation sensitivity indicator of four urban agglomerations of China  
1114 using Ozone Monitoring Instrument (OMI) satellite data and ground-based measurements,  
1115 *Science of The Total Environment*, 869, 161679,  
1116 <https://doi.org/10.1016/j.scitotenv.2023.161679>, 2023.

1117 Cohen, Y., Petetin, H., Thouret, V., Marécal, V., Josse, B., Clark, H., Sauvage, B., Fontaine,  
1118 A., Athier, G., Blot, R., Boulanger, D., Cousin, J. M., and Nédélec, P.: Climatology and long-  
1119 term evolution of ozone and carbon monoxide in the upper troposphere–lower stratosphere  
1120 (UTLS) at northern midlatitudes, as seen by IAGOS from 1995 to 2013, *Atmos. Chem. Phys.*,  
1121 18, 5415–5453, 10.5194/acp-18-5415-2018, 2018.

1122 Cooper, O. R., Parrish, D. D., Ziemke, J., Balashov, N. V., Cupeiro, M., Galbally, I. E., Gilge,  
1123 S., Horowitz, L., Jensen, N. R., Lamarque, J.-F., Naik, V., Oltmans, S. J., Schwab, J., Shindell,  
1124 D. T., Thompson, A. M., Thouret, V., Wang, Y., and Zbinden, R. M.: Global distribution and  
1125 trends of tropospheric ozone: An observation-based review, *Elementa: Science of the*  
1126 *Anthropocene*, 2, 10.12952/journal.elementa.000029, 2014.

1127 Cuesta, J., Kanaya, Y., Takigawa, M., Dufour, G., Eremenko, M., Foret, G., Miyazaki, K., and  
1128 Beekmann, M.: Transboundary ozone pollution across East Asia: daily evolution and  
1129 photochemical production analysed by IASI + GOME2 multispectral satellite observations and  
1130 models, *Atmos. Chem. Phys.*, 18, 9499–9525, 10.5194/acp-18-9499-2018, 2018.

1131 Cuesta, J., Costantino, L., Beekmann, M., Siour, G., Menut, L., Bessagnet, B., Landi, T. C.,  
1132 Dufour, G., and Eremenko, M.: Ozone pollution during the COVID-19 lockdown in the spring  
1133 of 2020 over Europe, analysed from satellite observations, in situ measurements, and models,  
1134 *Atmos. Chem. Phys.*, 22, 4471–4489, 10.5194/acp-22-4471-2022, 2022.

1135 Cuesta, J., Eremenko, M., Liu, X., Dufour, G., Cai, Z., Höpfner, M., von Clarmann, T., Sellitto,  
1136 P., Foret, G., Gaubert, B., Beekmann, M., Orphal, J., Chance, K., Spurr, R., and Flaud, J. M.:  
1137 Satellite observation of lowermost tropospheric ozone by multispectral synergism of IASI  
1138 thermal infrared and GOME-2 ultraviolet measurements over Europe, *Atmos. Chem. Phys.*,  
1139 13, 9675–9693, 10.5194/acp-13-9675-2013, 2013.

1140 De Smedt, I., Stavrou, T., Hendrick, F., Danckaert, T., Vlemmix, T., Pinardi, G., Theys, N.,  
1141 Lerot, C., Gielen, C., Vigouroux, C., Hermans, C., Fayt, C., Veefkind, P., Müller, J. F., and  
1142 Van Roozendaal, M.: Diurnal, seasonal and long-term variations of global formaldehyde  
1143 columns inferred from combined OMI and GOME-2 observations, *Atmos. Chem. Phys.*, 15,  
1144 12519–12545, 10.5194/acp-15-12519-2015, 2015.

1145 De Smedt, I., Theys, N., Yu, H., Danckaert, T., Lerot, C., Compennolle, S., Van Roozendaal,  
1146 M., Richter, A., Hilboll, A., Peters, E., Pedernana, M., Loyola, D., Beirle, S., Wagner, T.,  
1147 Eskes, H., van Geffen, J., Boersma, K. F., and Veefkind, P.: Algorithm theoretical baseline for

1148 formaldehyde retrievals from S5P TROPOMI and from the QA4ECV project, *Atmos. Meas.*  
 1149 *Tech.*, 11, 2395-2426, 10.5194/amt-11-2395-2018, 2018.

1150 De Smedt, I., Pinardi, G., Vigouroux, C., Compernelle, S., Bais, A., Benavent, N., Boersma,  
 1151 F., Chan, K. L., Donner, S., Eichmann, K. U., Hedelt, P., Hendrick, F., Irie, H., Kumar, V.,  
 1152 Lambert, J. C., Langerock, B., Lerot, C., Liu, C., Loyola, D., Piders, A., Richter, A., Rivera  
 1153 Cárdenas, C., Romahn, F., Ryan, R. G., Sinha, V., Theys, N., Vlietinck, J., Wagner, T., Wang,  
 1154 T., Yu, H., and Van Roozendael, M.: Comparative assessment of TROPOMI and OMI  
 1155 formaldehyde observations and validation against MAX-DOAS network column  
 1156 measurements, *Atmos. Chem. Phys.*, 21, 12561-12593, 10.5194/acp-21-12561-2021, 2021.

1157 Duncan, B. N., Yoshida, Y., Olson, J. R., Sillman, S., Martin, R. V., Lamsal, L., Hu, Y.,  
 1158 Pickering, K. E., Retscher, C., Allen, D. J., and Crawford, J. H.: Application of OMI  
 1159 observations to a space-based indicator of NO<sub>x</sub> and VOC controls on surface ozone formation,  
 1160 *Atmospheric Environment*, 44, 2213-2223, <https://doi.org/10.1016/j.atmosenv.2010.03.010>,  
 1161 2010.

1162 Edwards, J. M. and Slingo, A.: Studies with a flexible new radiation code. I: Choosing a  
 1163 configuration for a large-scale model, *Quarterly Journal of the Royal Meteorological Society*,  
 1164 122, 689-719, <https://doi.org/10.1002/qj.49712253107>, 1996.

1165 Edwards, D. P., Martínez-Alonso, S., Jo, D. S., Ortega, I., Emmons, L. K., Orlando, J. J.,  
 1166 Worden, H. M., Kim, J., Lee, H., Park, J., and Hong, H.: Quantifying the diurnal variation in  
 1167 atmospheric NO<sub>2</sub> from Geostationary Environment Monitoring Spectrometer (GEMS)  
 1168 observations, *Atmos. Chem. Phys.*, 24, 8943–8961, <https://doi.org/10.5194/acp-24-8943-2024>,  
 1169 2024.

1170 Elshorbany, Y., Ziemke, J., Strode, S., Petetin, H., Miyazaki, K., De Smedt, I., Pickering, K.,  
 1171 Seguel, R., Worden, H., Emmerichs, T., Taraborrelli, D., Cazorla, M., Fadnavis, S., Buchholz,  
 1172 R., Gaubert, B., Rojas, N., Nogueira, T., Salameh, T., and Huang, M.: Tropospheric Ozone  
 1173 Precursors: Global and Regional Distributions, Trends and Variability, *Atmos. Chem. Phys.*,  
 1174 24, 12225–12257, <https://doi.org/10.5194/acp-24-12225-2024>, 2024

1175 Emmons, L. K., Apel, E. C., Lamarque, J. F., Hess, P. G., Avery, M., Blake, D., Brune, W.,  
 1176 Campos, T., Crawford, J., DeCarlo, P. F., Hall, S., Heikes, B., Holloway, J., Jimenez, J. L.,  
 1177 Knapp, D. J., Kok, G., Mena-Carrasco, M., Olson, J., O'Sullivan, D., Sachse, G., Walega, J.,  
 1178 Weibring, P., Weinheimer, A., and Wiedinmyer, C.: Impact of Mexico City emissions on  
 1179 regional air quality from MOZART-4 simulations, *Atmos. Chem. Phys.*, 10, 6195-6212,  
 1180 10.5194/acp-10-6195-2010, 2010.

1181 EPA, O. U. Air Pollutant Emissions Trends Data. [https://www.epa.gov/air-emissions-](https://www.epa.gov/air-emissions-inventories/air-pollutant-emissions-trends-data)  
 1182 [inventories/air-pollutant-emissions-trends-data](https://www.epa.gov/air-emissions-inventories/air-pollutant-emissions-trends-data), 2023

1183 Fadnavis, S., Sabin, T. P., Rap, A., Müller, R., Kubin, A., and Heinold, B.: The impact of  
 1184 COVID-19 lockdown measures on the Indian summer monsoon, *Environmental Research*  
 1185 *Letters*, 16, 074054, 10.1088/1748-9326/ac109c, 2021a.

1186 Fadnavis, S., Heinold, B., Sabin, T. P., Kubin, A., Huang, K., Rap, A., and Müller, R.: Air  
 1187 pollution reductions caused by the COVID-19 lockdown open up a way to preserve the  
 1188 Himalayan glaciers, *Atmos. Chem. Phys.*, 23, 10439-10449, 10.5194/acp-23-10439-2023,  
 1189 2023.

1190 Fadnavis, S., Sabin, T. P., Roy, C., Rowlinson, M., Rap, A., Vernier, J.-P., and Sioris, C. E.:  
 1191 Elevated aerosol layer over South Asia worsens the Indian droughts, *Scientific Reports*, 9,  
 1192 10268, 10.1038/s41598-019-46704-9, 2019a.

1193 Fadnavis, S., Müller, R., Kalita, G., Rowlinson, M., Rap, A., Li, J. L. F., Gasparini, B., and  
 1194 Laakso, A.: The impact of recent changes in Asian anthropogenic emissions of SO<sub>2</sub> on sulfate  
 1195 loading in the upper troposphere and lower stratosphere and the associated radiative changes,  
 1196 *Atmos. Chem. Phys.*, 19, 9989-10008, 10.5194/acp-19-9989-2019, 2019b.

1197 Fadnavis, S., Chavan, P., Joshi, A., Sonbawne, S. M., Acharya, A., Devara, P. C. S., Rap, A.,  
 1198 Ploeger, F., and Müller, R.: Tropospheric warming over the northern Indian Ocean caused by  
 1199 South Asian anthropogenic aerosols: possible impact on the upper troposphere and lower  
 1200 stratosphere, *Atmos. Chem. Phys.*, 22, 7179-7191, 10.5194/acp-22-7179-2022, 2022.

1201 Fadnavis, S., Müller, R., Chakraborty, T., Sabin, T. P., Laakso, A., Rap, A., Griessbach, S.,  
 1202 Vernier, J.-P., and Tilmes, S.: The role of tropical volcanic eruptions in exacerbating Indian  
 1203 droughts, *Scientific Reports*, 11, 2714, 10.1038/s41598-021-81566-0, 2021b.

1204 Fiore, A. M., Hancock, S. E., Lamarque, J.-F., Correa, G. P., Chang, K.-L., Ru, M., Cooper,  
 1205 O., Gaudel, A., Polvani, L. M., Sauvage, B., and Ziemke, J. R.: Understanding recent  
 1206 tropospheric ozone trends in the context of large internal variability: a new perspective from  
 1207 chemistry-climate model ensembles, *Environmental Research: Climate*, 1, 025008,  
 1208 10.1088/2752-5295/ac9cc2, 2022.

1209 Fleming, Z. L., Doherty, R. M., von Schneidemesser, E., Malley, C. S., Cooper, O. R., Pinto,  
 1210 J. P., Colette, A., Xu, X., Simpson, D., Schultz, M. G., Lefohn, A. S., Hamad, S., Moolla, R.,  
 1211 Solberg, S., and Feng, Z.: Tropospheric Ozone Assessment Report: Present-day ozone  
 1212 distribution and trends relevant to human health, *Elementa: Science of the Anthropocene*, 6,  
 1213 10.1525/elementa.273, 2018.

1214 Forster, P., Storelvmo, T., Armour, K., Collins, W., Dufresne, J.-L., Frame, D., Lunt, D. J.,  
 1215 Mauritsen, T., Palmer, M. D., Watanabe, M., Wild, M., and Zhang, H.: The Earth's Energy  
 1216 Budget, Climate Feedbacks and Climate Sensitivity, in: *Climate Change 2021: The Physical  
 1217 Science Basis. Contribution of Working Group I to the Sixth Assessment Report of the  
 1218 Intergovernmental Panel on Climate Change* [Masson-Delmotte, V., P. Zhai, A. Pirani, S.L.  
 1219 Connors, C. Péan, S. Berger, N. Caud, Y. Chen, L. Goldfarb, M.I. Gomis, M. Huang, K.  
 1220 Leitzell, E. Lonnoy, J.B.R. Matthews, T.K. Maycock, T. Waterfield, O. Yelekçi, R. Yu, and B.  
 1221 Zhou (eds.)], edited by: Intergovernmental Panel on Climate, C., Cambridge University Press,  
 1222 Cambridge, 923-1054, DOI: 10.1017/9781009157896.009, 2021.

1223 Forster, P. M., Smith, C., Walsh, T., Lamb, W. F., Lamboll, R., Hall, B., Hauser, M., Ribes,  
 1224 A., Rosen, D., Gillett, N. P., Palmer, M. D., Rogelj, J., von Schuckmann, K., Trewin, B., Allen,  
 1225 M., Andrew, R., Betts, R. A., Borger, A., Boyer, T., Broersma, J. A., Buontempo, C., Burgess,  
 1226 S., Cagnazzo, C., Cheng, L., Friedlingstein, P., Gettelman, A., Gütschow, J., Ishii, M., Jenkins,  
 1227 S., Lan, X., Morice, C., Mühle, J., Kadow, C., Kennedy, J., Killick, R. E., Krummel, P. B.,  
 1228 Minx, J. C., Myhre, G., Naik, V., Peters, G. P., Pirani, A., Pongratz, J., Schleussner, C. F.,  
 1229 Seneviratne, S. I., Szopa, S., Thorne, P., Kovilakam, M. V. M., Majamäki, E., Jalkanen, J. P.,  
 1230 van Marle, M., Hoesly, R. M., Rohde, R., Schumacher, D., van der Werf, G., Vose, R.,  
 1231 Zickfeld, K., Zhang, X., Masson-Delmotte, V., and Zhai, P.: Indicators of Global Climate  
 1232 Change 2023: annual update of key indicators of the state of the climate system and human  
 1233 influence, *Earth Syst. Sci. Data*, 16, 2625-2658, 10.5194/essd-16-2625-2024, 2024.

1234 Gaudel, A., Bourgeois, I., Li, M., Chang, K. L., Ziemke, J., Sauvage, B., Stauffer, R. M.,  
1235 Thompson, A. M., Kollonige, D. E., Smith, N., Hubert, D., Keppens, A., Cuesta, J., Heue, K.  
1236 P., Veeffkind, P., Aikin, K., Peischl, J., Thompson, C. R., Ryerson, T. B., Frost, G. J.,  
1237 McDonald, B. C., and Cooper, O. R.: Tropical tropospheric ozone distribution and trends from  
1238 in situ and satellite data, *EGUsphere*, 2024, 1-51, 10.5194/egusphere-2023-3095, 2024.

1239 Gaudel, A., Cooper, O. R., Ancellet, G., Barret, B., Boynard, A., Burrows, J. P., Clerbaux, C.,  
1240 Coheur, P.-F., Cuesta, J., Cuevas, E., Doniki, S., Dufour, G., Ebojie, F., Foret, G., Garcia, O.,  
1241 Granados-Muñoz, M. J., Hannigan, J. W., Hase, F., Hassler, B., Huang, G., Hurtmans, D.,  
1242 Jaffe, D., Jones, N., Kalabokas, P., Kerridge, B., Kulawik, S., Latter, B., Leblanc, T., Le  
1243 Flochmoën, E., Lin, W., Liu, J., Liu, X., Mahieu, E., McClure-Begley, A., Neu, J. L., Osman,  
1244 M., Palm, M., Petetin, H., Petropavlovskikh, I., Querel, R., Rahpoe, N., Rozanov, A., Schultz,  
1245 M. G., Schwab, J., Siddans, R., Smale, D., Steinbacher, M., Tanimoto, H., Tarasick, D. W.,  
1246 Thouret, V., Thompson, A. M., Trickl, T., Weatherhead, E., Wespes, C., Worden, H. M.,  
1247 Vigouroux, C., Xu, X., Zeng, G., and Ziemke, J.: Tropospheric Ozone Assessment Report:  
1248 Present-day distribution and trends of tropospheric ozone relevant to climate and global  
1249 atmospheric chemistry model evaluation, *Elementa: Science of the Anthropocene*, 6,  
1250 10.1525/elementa.291, 2018.

1251 Glissenaar, I. A., Anglou, I., Boersma, K. F., & Eskes, H., ESA CCI+ TROPOMI L3 monthly  
1252 mean NO<sub>2</sub> columns [Data set]. Royal Netherlands Meteorological Institute (KNMI).  
1253 <https://doi.org/10.21944/CCI-NO2-TROPOMI-L3>, 2024

1254 Goldberg, D. L., Anenberg, S. C., Kerr, G. H., Mohegh, A., Lu, Z., and Streets, D. G.:  
1255 TROPOMI NO<sub>2</sub> in the United States: A Detailed Look at the Annual Averages, Weekly  
1256 Cycles, Effects of Temperature, and Correlation With Surface NO<sub>2</sub> Concentrations, *Earth's*  
1257 *Future*, 9, e2020EF001665, <https://doi.org/10.1029/2020EF001665>, 2021.

1258 Griffiths, P. T., Murray, L. T., Zeng, G., Shin, Y. M., Abraham, N. L., Archibald, A. T., Deushi,  
1259 M., Emmons, L. K., Galbally, I. E., Hassler, B., Horowitz, L. W., Keeble, J., Liu, J., Moeini,  
1260 O., Naik, V., O'Connor, F. M., Oshima, N., Tarasick, D., Tilmes, S., Turnock, S. T., Wild, O.,  
1261 Young, P. J., and Zanis, P.: Tropospheric ozone in CMIP6 simulations, *Atmos. Chem. Phys.*,  
1262 21, 4187-4218, 10.5194/acp-21-4187-2021, 2021.

1263 Guan, J., Jin, B., Ding, Y., Wang, W., Li, G., and Ciren, P.: Global Surface HCHO Distribution  
1264 Derived from Satellite Observations with Neural Networks Technique, *Remote Sensing*, 13,  
1265 4055, 2021.

1266 Guenther, A. B., Jiang, X., Heald, C. L., Sakulyanontvittaya, T., Duhl, T., Emmons, L. K., and  
1267 Wang, X.: The Model of Emissions of Gases and Aerosols from Nature version 2.1  
1268 (MEGAN2.1): an extended and updated framework for modeling biogenic emissions, *Geosci.*  
1269 *Model Dev.*, 5, 1471-1492, 10.5194/gmd-5-1471-2012, 2012.

1270 Gulev, S. K., Thorne, P. W., Ahn, J., Dentener, F. J., Domingues, C. M., Gerland, S., Gong,  
1271 D., Kaufman, D. S., Nnamchi, H. C., Quaas, J., Rivera, J. A., Sathyendranath, S., Smith, S. L.,  
1272 Trewin, B., von Schuckmann, K., and Vose, R. S.: Changing State of the Climate System, in:  
1273 *Climate Change 2021 – The Physical Science Basis: Working Group I Contribution to the Sixth*  
1274 *Assessment Report of the Intergovernmental Panel on Climate Change* [Masson-Delmotte, V.,  
1275 P. Zhai, A. Pirani, S.L. Connors, C. Péan, S. Berger, N. Caud, Y. Chen, L. Goldfarb, M.I.  
1276 Gomis, M. Huang, K. Leitzell, E. Lonnoy, J.B.R. Matthews, T.K. Maycock, T. Waterfield, O.

1277 Yelekçi, R. Yu, and B. Zhou (eds.)], edited by: Intergovernmental Panel on Climate, C.,  
1278 Cambridge University Press, Cambridge, 287-422, DOI: 10.1017/9781009157896.004, 2021.

1279 Henrot, A. J., Stanelle, T., Schröder, S., Siegenthaler, C., Taraborrelli, D., and Schultz, M. G.:  
1280 Implementation of the MEGAN (v2.1) biogenic emission model in the ECHAM6-HAMMOZ  
1281 chemistry climate model, *Geosci. Model Dev.*, 10, 903-926, 10.5194/gmd-10-903-2017, 2017.

1282 Hoffmann, L. and Spang, R.: An assessment of tropopause characteristics of the ERA5 and  
1283 ERA-Interim meteorological reanalyses, *Atmos. Chem. Phys.*, 22, 4019–4046,  
1284 <https://doi.org/10.5194/acp-22-4019-2022>, 2022.

1285 Jin, X. and Holloway, T.: Spatial and temporal variability of ozone sensitivity over China  
1286 observed from the Ozone Monitoring Instrument, *Journal of Geophysical Research: Atmospheres*,  
1287 120, 7229-7246, <https://doi.org/10.1002/2015JD023250>, 2015.

1288 Jin, X., Fiore, A., Boersma, K. F., Smedt, I. D., and Valin, L.: Inferring Changes in  
1289 Summertime Surface Ozone–NO<sub>x</sub>–VOC Chemistry over U.S. Urban Areas from Two Decades  
1290 of Satellite and Ground-Based Observations, *Environmental Science & Technology*, 54, 6518-  
1291 6529, 10.1021/acs.est.9b07785, 2020.

1292 Jin, X., Fiore, A. M., Murray, L. T., Valin, L. C., Lamsal, L. N., Duncan, B., Folkert Boersma,  
1293 K., De Smedt, I., Abad, G. G., Chance, K., and Tonnesen, G. S.: Evaluating a Space-Based  
1294 Indicator of Surface Ozone-NO-VOC Sensitivity Over Midlatitude Source Regions and  
1295 Application to Decadal Trends, *Journal of Geophysical Research: Atmospheres*, 122, 10,439-  
1296 410,461, <https://doi.org/10.1002/2017JD026720>, 2017.

1297 Johnson, M. S., Philip, S., Meech, S., Kumar, R., Sorek-Hamer, M., Shiga, Y. P., and Jung, J.:  
1298 Insights into the long-term (2005–2021) spatiotemporal evolution of summer ozone production  
1299 sensitivity in the Northern Hemisphere derived with the Ozone Monitoring Instrument (OMI),  
1300 *Atmos. Chem. Phys.*, 24, 10363-10384, 10.5194/acp-24-10363-2024, 2024.

1301 Kinnison, D. E., Brasseur, G. P., Walters, S., Garcia, R. R., Marsh, D. R., Sassi, F., Harvey, V.  
1302 L., Randall, C. E., Emmons, L., Lamarque, J. F., Hess, P., Orlando, J. J., Tie, X. X., Randel,  
1303 W., Pan, L. L., Gettelman, A., Granier, C., Diehl, T., Niemeier, U., and Simmons, A. J.:  
1304 Sensitivity of chemical tracers to meteorological parameters in the MOZART-3 chemical  
1305 transport model, *Journal of Geophysical Research: Atmospheres*, 112,  
1306 <https://doi.org/10.1029/2006JD007879>, 2007.

1307 Kleinman, L. I.: Low and high NO<sub>x</sub> tropospheric photochemistry, *Journal of Geophysical Research: Atmospheres*, 99, 16831-16838, <https://doi.org/10.1029/94JD01028>, 1994.

1309 Kumar, V., Beirle, S., Dörner, S., Mishra, A. K., Donner, S., Wang, Y., Sinha, V., and Wagner,  
1310 T.: Long-term MAX-DOAS measurements of NO<sub>2</sub>, HCHO, and aerosols and evaluation of  
1311 corresponding satellite data products over Mohali in the Indo-Gangetic Plain, *Atmos. Chem. Phys.*, 20, 14183-14235, 10.5194/acp-20-14183-2020, 2020.

1313 Lamarque, J. F., Emmons, L. K., Hess, P. G., Kinnison, D. E., Tilmes, S., Vitt, F., Heald, C.  
1314 L., Holland, E. A., Lauritzen, P. H., Neu, J., Orlando, J. J., Rasch, P. J., and Tyndall, G. K.:  
1315 CAM-chem: description and evaluation of interactive atmospheric chemistry in the  
1316 Community Earth System Model, *Geosci. Model Dev.*, 5, 369-411, 10.5194/gmd-5-369-2012,  
1317 2012.



1318 Lamarque, J. F., Bond, T. C., Eyring, V., Granier, C., Heil, A., Klimont, Z., Lee, D., Lioussé,  
 1319 C., Mieville, A., Owen, B., Schultz, M. G., Shindell, D., Smith, S. J., Stehfest, E., Van  
 1320 Aardenne, J., Cooper, O. R., Kainuma, M., Mahowald, N., McConnell, J. R., Naik, V., Riahi,  
 1321 K., and van Vuuren, D. P.: Historical (1850–2000) gridded anthropogenic and biomass burning  
 1322 emissions of reactive gases and aerosols: methodology and application, *Atmos. Chem. Phys.*,  
 1323 10, 7017-7039, 10.5194/acp-10-7017-2010, 2010.

1324 Lamsal, L. N., Krotkov, N. A., Vasilkov, A., Marchenko, S., Qin, W., Yang, E. S., Fasnacht,  
 1325 Z., Joiner, J., Choi, S., Haffner, D., Swartz, W. H., Fisher, B., and Bucsela, E.: Ozone  
 1326 Monitoring Instrument (OMI) Aura nitrogen dioxide standard product version 4.0 with  
 1327 improved surface and cloud treatments, *Atmos. Meas. Tech.*, 14, 455-479, 10.5194/amt-14-  
 1328 455-2021, 2021.

1329 Lefohn, A. S., Malley, C. S., Simon, H., Wells, B., Xu, X., Zhang, L., and Wang, T.: Responses  
 1330 of human health and vegetation exposure metrics to changes in ozone concentration  
 1331 distributions in the European Union, United States, and China, *Atmospheric Environment*, 152,  
 1332 123-145, <https://doi.org/10.1016/j.atmosenv.2016.12.025>, 2017.

1333 Li, M., Kurokawa, J., Zhang, Q., Woo, J. H., Morikawa, T., Chatani, S., Lu, Z., Song, Y., Geng,  
 1334 G., Hu, H., Kim, J., Cooper, O. R., and McDonald, B. C.: MIXv2: a long-term mosaic emission  
 1335 inventory for Asia (2010–2017), *Atmos. Chem. Phys.*, 24, 3925-3952, 10.5194/acp-24-3925-  
 1336 2024, 2024.

1337 Li, S., Yang, Y., Wang, H., Li, P., Li, K., Ren, L., Wang, P., Li, B., Mao, Y., and Liao, H.:  
 1338 Rapid increase in tropospheric ozone over Southeast Asia attributed to changes in precursor  
 1339 emission source regions and sectors, *Atmospheric Environment*, 304, 119776,  
 1340 <https://doi.org/10.1016/j.atmosenv.2023.119776>, 2023.

1341 Lin, M., Horowitz, L. W., Oltmans, S. J., Fiore, A. M., and Fan, S.: Tropospheric ozone trends  
 1342 at Mauna Loa Observatory tied to decadal climate variability, *Nature Geoscience*, 7, 136-143,  
 1343 10.1038/ngeo2066, 2014.

1344 Liu, J., Strode, S. A., Liang, Q., Oman, L. D., Colarco, P. R., Fleming, E. L., Manyin, M. E.,  
 1345 Douglass, A. R., Ziemke, J. R., Lamsal, L. N., and Li, C.: Change in Tropospheric Ozone in  
 1346 the Recent Decades and Its Contribution to Global Total Ozone, *Journal of Geophysical*  
 1347 *Research: Atmospheres*, 127, e2022JD037170, <https://doi.org/10.1029/2022JD037170>, 2022.

1348 Lu, X., Zhang, L., Liu, X., Gao, M., Zhao, Y., and Shao, J.: Lower tropospheric ozone over  
 1349 India and its linkage to the South Asian monsoon, *Atmos. Chem. Phys.*, 18, 3101-3118,  
 1350 10.5194/acp-18-3101-2018, 2018.

1351 Mahajan, A. S., De Smedt, I., Biswas, M. S., Ghude, S., Fadnavis, S., Roy, C., and van  
 1352 Roozendaal, M.: Inter-annual variations in satellite observations of nitrogen dioxide and  
 1353 formaldehyde over India, *Atmospheric Environment*, 116, 194-201,  
 1354 <https://doi.org/10.1016/j.atmosenv.2015.06.004>, 2015.

1355 Martin, R. V., Fiore, A. M., and Van Donkelaar, A.: Space-based diagnosis of surface ozone  
 1356 sensitivity to anthropogenic emissions, *Geophysical Research Letters*, 31,  
 1357 <https://doi.org/10.1029/2004GL019416>, 2004.

1358 Matricardi, M., Chevallier, F., Kelly, G., and Thépaut, J.-N.: An improved general fast radiative  
1359 transfer model for the assimilation of radiance observations, *Quarterly Journal of the Royal*  
1360 *Meteorological Society*, 130, 153-173, <https://doi.org/10.1256/qj.02.181>, 2004.

1361 Mills, G., Pleijel, H., Malley, C. S., Sinha, B., Cooper, O. R., Schultz, M. G., Neufeld, H. S.,  
1362 Simpson, D., Sharps, K., Feng, Z., Gerosa, G., Harmens, H., Kobayashi, K., Saxena, P.,  
1363 Paoletti, E., Sinha, V., and Xu, X.: Tropospheric Ozone Assessment Report: Present-day  
1364 tropospheric ozone distribution and trends relevant to vegetation, *Elementa: Science of the*  
1365 *Anthropocene*, 6, 10.1525/elementa.302, 2018.

1366 Monks, P. S., Archibald, A. T., Colette, A., Cooper, O., Coyle, M., Derwent, R., Fowler, D.,  
1367 Granier, C., Law, K. S., Mills, G. E., Stevenson, D. S., Tarasova, O., Thouret, V., von  
1368 Schneidemesser, E., Sommariva, R., Wild, O., and Williams, M. L.: Tropospheric ozone and  
1369 its precursors from the urban to the global scale from air quality to short-lived climate forcer,  
1370 *Atmos. Chem. Phys.*, 15, 8889-8973, 10.5194/acp-15-8889-2015, 2015.

1371

1372 O3 (IASI+GOME2) – IASI portal: [https://iasi.aeris-data.fr/o3\\_iago2/](https://iasi.aeris-data.fr/o3_iago2/), last access: 28 May 2024

1373 Okamoto, S., Cuesta, J., Beekmann, M., Dufour, G., Eremenko, M., Miyazaki, K., Boonne, C.,  
1374 Tanimoto, H., and Akimoto, H.: Impact of different sources of precursors on an ozone pollution  
1375 outbreak over Europe analysed with IASI+GOME2 multispectral satellite observations and  
1376 model simulations, *Atmos. Chem. Phys.*, 23, 7399-7423, 10.5194/acp-23-7399-2023, 2023.

1377 Pope, R. J., Rap, A., Pimlott, M. A., Barret, B., Le Flochmoen, E., Kerridge, B. J., Siddans, R.,  
1378 Latter, B. G., Ventress, L. J., Boynard, A., Retscher, C., Feng, W., Rigby, R., Dhomse, S. S.,  
1379 Wespes, C., and Chipperfield, M. P.: Quantifying the tropospheric ozone radiative effect and  
1380 its temporal evolution in the satellite era, *Atmos. Chem. Phys.*, 24, 3613-3626, 10.5194/acp-  
1381 24-3613-2024, 2024.

1382 Prather, M., and Zhu X., Lifetimes and timescales of tropospheric ozone, Lifetimes and  
1383 timescales of tropospheric ozone. *Elem*, 12, 1, 2024, doi:10.1525/elementa.2023.00112.

1384 Putero, D., Cristofanelli, P., Chang, K. L., Dufour, G., Beachley, G., Couret, C., Effertz, P.,  
1385 Jaffe, D. A., Kubistin, D., Lynch, J., Petropavlovskikh, I., Puchalski, M., Sharac, T., Sive, B.  
1386 C., Steinbacher, M., Torres, C., and Cooper, O. R.: Fingerprints of the COVID-19 economic  
1387 downturn and recovery on ozone anomalies at high-elevation sites in North America and  
1388 western Europe, *Atmos. Chem. Phys.*, 23, 15693-15709, 10.5194/acp-23-15693-2023, 2023.

1389 Rap, A., Richards, N. A. D., Forster, P. M., Monks, S. A., Arnold, S. R., and Chipperfield, M.  
1390 P.: Satellite constraint on the tropospheric ozone radiative effect, *Geophysical Research*  
1391 *Letters*, 42, 5074-5081, <https://doi.org/10.1002/2015GL064037>, 2015.

1392 Rast, S., Schultz, M. G., Bey, I., van Noije, T., Aghedo, A. M., Brasseur, G. P., Diehl, T., Esch,  
1393 M., Ganzeveld, L., Kirchner, I., Kornbluh, L., Rhodin, A., Roeckner, E., Schmidt, H.,  
1394 Schroder, S., Schulzweida, U., Stier, P., Thomas, K., and Walters, S.: Evaluation of the  
1395 tropospheric chemistry general circulation model ECHAM5–MOZ and its application to the  
1396 analysis of the chemical composition of the troposphere with an emphasis on the late RETRO  
1397 period 1990–2000, *Max-Planck-Institut für Meteorologie, Hamburg* 114, 2014.

- 1398 Reick, C. H., Raddatz, T., Brovkin, V., and Gayler, V.: Representation of natural and  
1399 anthropogenic land cover change in MPI-ESM, *Journal of Advances in Modeling Earth*  
1400 *Systems*, 5, 459-482, <https://doi.org/10.1002/jame.20022>, 2013.
- 1401 Ren, J., Guo, F., and Xie, S.: Diagnosing ozone–NO<sub>x</sub>–VOC sensitivity and revealing causes  
1402 of ozone increases in China based on 2013–2021 satellite retrievals, *Atmos. Chem. Phys.*, 22,  
1403 15035-15047, 10.5194/acp-22-15035-2022, 2022.
- 1404 Riese, M. and Ploeger, F. and Rap, A. and Vogel, B. and Konopka, P. and Dameris, M. and  
1405 Forster, P.: Impact of uncertainties in atmospheric mixing on simulated UTLS composition and  
1406 related radiative effects, *J. Geophys. Res.*, 117, D16305, 10.1029/2012JD017751, 2012
- 1407 Rosanka, S., Franco, B., Clarisse, L., Coheur, P. F., Pozzer, A., Wahner, A., and Taraborrelli,  
1408 D.: The impact of organic pollutants from Indonesian peatland fires on the tropospheric and  
1409 lower stratospheric composition, *Atmos. Chem. Phys.*, 21, 11257-11288, 10.5194/acp-21-  
1410 11257-2021, 2021.
- 1411 Rothman, L. S., Jacquemart, D., Barbe, A., Chris Benner, D., Birk, M., Brown, L. R., Carleer,  
1412 M. R., Chackerian, C., Chance, K., Coudert, L. H., Dana, V., Devi, V. M., Flaud, J. M.,  
1413 Gamache, R. R., Goldman, A., Hartmann, J. M., Jucks, K. W., Maki, A. G., Mandin, J. Y.,  
1414 Massie, S. T., Orphal, J., Perrin, A., Rinsland, C. P., Smith, M. A. H., Tennyson, J., Tolchenov,  
1415 R. N., Toth, R. A., Vander Auwera, J., Varanasi, P., and Wagner, G.: The HITRAN 2004  
1416 molecular spectroscopic database, *Journal of Quantitative Spectroscopy and Radiative*  
1417 *Transfer*, 96, 139-204, <https://doi.org/10.1016/j.jqsrt.2004.10.008>, 2005.
- 1418 Rowlinson, M. J., Rap, A., Hamilton, D. S., Pope, R. J., Hantson, S., Arnold, S. R., Kaplan, J.  
1419 O., Arneth, A., Chipperfield, M. P., Forster, P. M., and Nieradzik, L.: Tropospheric ozone  
1420 radiative forcing uncertainty due to pre-industrial fire and biogenic emissions, *Atmos. Chem.*  
1421 *Phys.*, 20, 10937-10951, 10.5194/acp-20-10937-2020, 2020.
- 1422 Saunders, R., Matricardi, M., and Brunel, P.: An improved fast radiative transfer model for  
1423 assimilation of satellite radiance observations, *Quarterly Journal of the Royal Meteorological*  
1424 *Society*, 125, 1407-1425, <https://doi.org/10.1002/qj.1999.49712555615>, 1999.
- 1425 Schroeder, J. R., Crawford, J. H., Fried, A., Walega, J., Weinheimer, A., Wisthaler, A., Müller,  
1426 M., Mikoviny, T., Chen, G., Shook, M., Blake, D. R., and Tonnesen, G. S.: New insights into  
1427 the column CH<sub>2</sub>O/NO<sub>2</sub> ratio as an indicator of near-surface ozone sensitivity, *Journal of*  
1428 *Geophysical Research: Atmospheres*, 122, 8885-8907, <https://doi.org/10.1002/2017JD026781>,  
1429 2017.
- 1430 Schultz, M. G., Stadtler, S., Schröder, S., Taraborrelli, D., Franco, B., Krefting, J., Henrot, A.,  
1431 Ferrachat, S., Lohmann, U., Neubauer, D., Siegenthaler-Le Drian, C., Wahl, S., Kokkola, H.,  
1432 Kühn, T., Rast, S., Schmidt, H., Stier, P., Kinnison, D., Tyndall, G. S., Orlando, J. J., and  
1433 Wespes, C.: The chemistry–climate model ECHAM6.3-HAM2.3-MOZ1.0, *Geosci. Model*  
1434 *Dev.*, 11, 1695-1723, 10.5194/gmd-11-1695-2018, 2018.
- 1435 Schultz, M. G., Schröder, S., Lyapina, O., Cooper, O. R., Galbally, I., Petropavlovskikh, I., von  
1436 Schneidemesser, E., Tanimoto, H., Elshorbany, Y., Naja, M., Seguel, R. J., Dauert, U.,  
1437 Eckhardt, P., Feigenspan, S., Fiebig, M., Hjellbrekke, A.-G., Hong, Y.-D., Kjeld, P. C., Koide,  
1438 H., Lear, G., Tarasick, D., Ueno, M., Wallasch, M., Baumgardner, D., Chuang, M.-T., Gillett,  
1439 R., Lee, M., Molloy, S., Moolla, R., Wang, T., Sharps, K., Adame, J. A., Ancellet, G., Apadula,  
1440 F., Artaxo, P., Barlasina, M. E., Bogucka, M., Bonasoni, P., Chang, L., Colomb, A., Cuevas-

1441 Agulló, E., Cupeiro, M., Degorska, A., Ding, A., Fröhlich, M., Frolova, M., Gadhavi, H.,  
 1442 Gheusi, F., Gilge, S., Gonzalez, M. Y., Gros, V., Hamad, S. H., Helmig, D., Henriques, D.,  
 1443 Hermansen, O., Holla, R., Hueber, J., Im, U., Jaffe, D. A., Komala, N., Kubistin, D., Lam, K.-  
 1444 S., Laurila, T., Lee, H., Levy, I., Mazzoleni, C., Mazzoleni, L. R., McClure-Begley, A.,  
 1445 Mohamad, M., Murovec, M., Navarro-Comas, M., Nicodim, F., Parrish, D., Read, K. A., Reid,  
 1446 N., Ries, L., Saxena, P., Schwab, J. J., Scorgie, Y., Senik, I., Simmonds, P., Sinha, V.,  
 1447 Skorokhod, A. I., Spain, G., Spangl, W., Spoor, R., Springston, S. R., Steer, K., Steinbacher,  
 1448 M., Suharguniyawan, E., Torre, P., Trickl, T., Weili, L., Weller, R., Xiaobin, X., Xue, L., and  
 1449 Zhiqiang, M.: Tropospheric Ozone Assessment Report: Database and metrics data of global  
 1450 surface ozone observations, *Elementa: Science of the Anthropocene*, 5, 10.1525/elementa.244,  
 1451 2017.

1452 Scott, C. E., Monks, S. A., Spracklen, D. V., Arnold, S. R., Forster, P. M., Rap, A., Äijälä, M.,  
 1453 Artaxo, P., Carslaw, K. S., Chipperfield, M. P., Ehn, M., Gilardoni, S., Heikkinen, L., Kulmala,  
 1454 M., Petäjä, T., Reddington, C. L. S., Rizzo, L. V., Swietlicki, E., Vignati, E., and Wilson, C.:  
 1455 Impact on short-lived climate forcers increases projected warming due to deforestation, *Nature*  
 1456 *Communications*, 9, 157, 10.1038/s41467-017-02412-4, 2018.

1457 Sillman, S.: The use of NO<sub>x</sub>, H<sub>2</sub>O<sub>2</sub>, and HNO<sub>3</sub> as indicators for ozone-NO<sub>x</sub>-hydrocarbon  
 1458 sensitivity in urban locations, *Journal of Geophysical Research: Atmospheres*, 100, 14175-  
 1459 14188, <https://doi.org/10.1029/94JD02953>, 1995.

1460 Sillman, S., Logan, J. A., and Wofsy, S. C.: The sensitivity of ozone to nitrogen oxides and  
 1461 hydrocarbons in regional ozone episodes, *Journal of Geophysical Research: Atmospheres*, 95,  
 1462 1837-1851, <https://doi.org/10.1029/JD095iD02p01837>, 1990.

1463 Sofieva, V. F., Tamminen, J., Kyrölä, E., Mielonen, T., Veefkind, P., Hassler, B., and Bodeker,  
 1464 G. E.: A novel tropopause-related climatology of ozone profiles, *Atmos. Chem. Phys.*, 14, 283-  
 1465 299, 10.5194/acp-14-283-2014, 2014.

1466 Sourì, A. H., Choi, Y., Jeon, W., Woo, J.-H., Zhang, Q., and Kurokawa, J.-i.: Remote sensing  
 1467 evidence of decadal changes in major tropospheric ozone precursors over East Asia, *Journal of*  
 1468 *Geophysical Research - Atmospheres*, 122, 2474-2492,  
 1469 <https://doi.org/10.1002/2016JD025663>, 2017.

1470 Stadtler, S., Simpson, D., Schröder, S., Taraborrelli, D., Bott, A., and Schultz, M.: Ozone  
 1471 impacts of gas-aerosol uptake in global chemistry transport models, *Atmos. Chem. Phys.*, 18,  
 1472 3147-3171, 10.5194/acp-18-3147-2018, 2018.

1473 Steinbrecht, W., Kubistin, D., Plass-Dülmer, C., Davies, J., Tarasick, D. W., von der Gathen,  
 1474 P., Deckelmann, H., Jepsen, N., Kivi, R., Lyall, N., Palm, M., Notholt, J., Kois, B., Oelsner,  
 1475 P., Allaart, M., Pithers, A., Gill, M., Van Malderen, R., Delcloo, A. W., Sussmann, R., Mahieu,  
 1476 E., Servais, C., Romanens, G., Stübi, R., Ancellet, G., Godin-Beekmann, S., Yamanouchi, S.,  
 1477 Strong, K., Johnson, B., Cullis, P., Petropavlovskikh, I., Hannigan, J. W., Hernandez, J.-L.,  
 1478 Diaz Rodriguez, A., Nakano, T., Chouza, F., Leblanc, T., Torres, C., Garcia, O., Röhling, A.  
 1479 N., Schneider, M., Blumenstock, T., Tully, M., Paton-Walsh, C., Jones, N., Querel, R., Strahan,  
 1480 S., Stauffer, R. M., Thompson, A. M., Inness, A., Engelen, R., Chang, K.-L., and Cooper, O.  
 1481 R.: COVID-19 Crisis Reduces Free Tropospheric Ozone Across the Northern Hemisphere,  
 1482 *Geophysical Research Letters*, 48, e2020GL091987, <https://doi.org/10.1029/2020GL091987>,  
 1483 2021.

1484 Stevens, B., Giorgetta, M., Esch, M., Mauritsen, T., Crueger, T., Rast, S., Salzmann, M.,  
1485 Schmidt, H., Bader, J., Block, K., Brokopf, R., Fast, I., Kinne, S., Kornblueh, L., Lohmann,  
1486 U., Pincus, R., Reichler, T., and Roeckner, E.: Atmospheric component of the MPI-M Earth  
1487 System Model: ECHAM6, *Journal of Advances in Modeling Earth Systems*, 5, 146-172,  
1488 10.1002/jame.20015, 2013.

1489 Stevenson, D. S., Dentener, F. J., Schultz, M. G., Ellingsen, K., van Noije, T. P. C., Wild, O.,  
1490 Zeng, G., Amann, M., Atherton, C. S., Bell, N., Bergmann, D. J., Bey, I., Butler, T., Cofala, J.,  
1491 Collins, W. J., Derwent, R. G., Doherty, R. M., Drevet, J., Eskes, H. J., Fiore, A. M., Gauss,  
1492 M., Hauglustaine, D. A., Horowitz, L. W., Isaksen, I. S. A., Krol, M. C., Lamarque, J. F.,  
1493 Lawrence, M. G., Montanaro, V., Müller, J. F., Pitari, G., Prather, M. J., Pyle, J. A., Rast, S.,  
1494 Rodriguez, J. M., Sanderson, M. G., Savage, N. H., Shindell, D. T., Strahan, S. E., Sudo, K.,  
1495 and Szopa, S.: Multimodel ensemble simulations of present-day and near-future tropospheric  
1496 ozone, *Journal of Geophysical Research-Atmospheres*, 111, 10.1029/2005JD006338, 2006.

1497 Surl, L., Palmer, P. I., and González Abad, G.: Which processes drive observed variations of  
1498 HCHO columns over India?, *Atmos. Chem. Phys.*, 18, 4549-4566, 10.5194/acp-18-4549-2018,  
1499 2018.

1500 Szopa, S., Naik, V., Adhikary, B., Artaxo, P., Bernsten, T., Collins, W. D., Fuzzi, S., Gallardo,  
1501 L., Kiendler-Scharr, A., Klimont, Z., Liao, H., Unger, N., and Zanis, P.: Short-lived Climate  
1502 Forcers, in: *Climate Change 2021: The Physical Science Basis. Contribution of Working Group*  
1503 *I to the Sixth Assessment Report of the Intergovernmental Panel on Climate Change* [Masson-  
1504 Delmotte, V., P. Zhai, A. Pirani, S.L. Connors, C. Péan, S. Berger, N. Caud, Y. Chen, L.  
1505 Goldfarb, M.I. Gomis, M. Huang, K. Leitzell, E. Lonnoy, J.B.R. Matthews, T.K. Maycock, T.  
1506 Waterfield, O. Yelekçi, R. Yu, and B. Zhou (eds.)], edited by: Intergovernmental Panel on  
1507 Climate, C., Cambridge University Press, Cambridge, 817-922, DOI:  
1508 10.1017/9781009157896.008, 2021.

1509 Taraborrelli, D., Cabrera-Perez, D., Bacer, S., Gromov, S., Lelieveld, J., Sander, R., and  
1510 Pozzer, A.: Influence of aromatics on tropospheric gas-phase composition, *Atmos. Chem.*  
1511 *Phys.*, 21, 2615-2636, 10.5194/acp-21-2615-2021, 2021.

1512 Tarasick, D. W., Carey-Smith, T. K., Hocking, W. K., Moeini, O., He, H., Liu, J., Osman, M.  
1513 K., Thompson, A. M., Johnson, B. J., Oltmans, S. J., and Merrill, J. T.: Quantifying  
1514 stratosphere-troposphere transport of ozone using balloon-borne ozone sondes, radar wind  
1515 profilers and trajectory models, *Atmospheric Environment*, 198, 496-509,  
1516 <https://doi.org/10.1016/j.atmosenv.2018.10.040>, 2019.

1517 Van Vuuren, D. P., Edmonds, J., Kainuma, M., Riahi, K., Thomson, A., Hibbard, K., Hurtt, G.  
1518 C., Kram, T., Krey, V., Lamarque, J.-F., Masui, T., Meinshausen, M., Nakicenovic, N., Smith,  
1519 S. J., and Rose, S. K.: The representative concentration pathways: an overview, *Climatic*  
1520 *Change*, 109, 5, 10.1007/s10584-011-0148-z, 2011.

1521 Veefkind, J. P., Aben, I., McMullan, K., Förster, H., de Vries, J., Otter, G., Claas, J., Eskes, H.  
1522 J., de Haan, J. F., Kleipool, Q., van Weele, M., Hasekamp, O., Hoogeveen, R., Landgraf, J.,  
1523 Snel, R., Tol, P., Ingmann, P., Voors, R., Kruizinga, B., Vink, R., Visser, H., and Levelt, P. F.:  
1524 TROPOMI on the ESA Sentinel-5 Precursor: A GMES mission for global observations of the  
1525 atmospheric composition for climate, air quality and ozone layer applications, *Remote Sensing*  
1526 *of Environment*, 120, 70-83, <https://doi.org/10.1016/j.rse.2011.09.027>, 2012.

1527 Verstraeten, W. W., Neu, J. L., Williams, J. E., Bowman, K. W., Worden, J. R., and Boersma,  
1528 K. F.: Rapid increases in tropospheric ozone production and export from China, *Nature*  
1529 *Geoscience*, 8, 690-695, 10.1038/ngeo2493, 2015.

1530 Vignati, E., Wilson, J., and Stier, P.: M7: An efficient size-resolved aerosol microphysics  
1531 module for large-scale aerosol transport models, *Journal of Geophysical Research*,  
1532 *Atmospheres*, 109, 10.1029/2003JD004485, 2004.

1533 Wang, Y., Zhao, Y., Liu, Y. *et al.* Sustained emission reductions have restrained the ozone  
1534 pollution over China. *Nat. Geosci.* **16**, 967–974 (2023). [https://doi.org/10.1038/s41561-023-](https://doi.org/10.1038/s41561-023-01284-2)  
1535 01284-2

1536 Wang, H., Lu, X., Jacob, D. J., Cooper, O. R., Chang, K. L., Li, K., Gao, M., Liu, Y., Sheng,  
1537 B., Wu, K., Wu, T., Zhang, J., Sauvage, B., Nédélec, P., Blot, R., and Fan, S.: Global  
1538 tropospheric ozone trends, attributions, and radiative impacts in 1995–2017: an integrated  
1539 analysis using aircraft (IAGOS) observations, ozone sonde, and multi-decadal chemical model  
1540 simulations, *Atmos. Chem. Phys.*, 22, 13753-13782, 10.5194/acp-22-13753-2022, 2022.

1541 Wang, W., van der A, R., Ding, J., van Weele, M., and Cheng, T.: Spatial and temporal changes  
1542 of the ozone sensitivity in China based on satellite and ground-based observations, *Atmos.*  
1543 *Chem. Phys.*, 21, 7253-7269, 10.5194/acp-21-7253-2021, 2021.

1544 Wang, Y., Lampel, J., Xie, P., Beirle, S., Li, A., Wu, D., and Wagner, T.: Ground-based MAX-  
1545 DOAS observations of tropospheric aerosols, NO<sub>2</sub>, SO<sub>2</sub> and HCHO in Wuxi, China, from  
1546 2011 to 2014, *Atmos. Chem. Phys.*, 17, 2189-2215, 10.5194/acp-17-2189-2017, 2017.

1547 WMO, Meteorology – A three-dimensional science, World Meteorological Organization,  
1548 Bulletin 6, (Oct), 134–138, 1957.

1549 Young, P. J., Naik, V., Fiore, A. M., Gaudel, A., Guo, J., Lin, M. Y., Neu, J. L., Parrish, D. D.,  
1550 Rieder, H. E., Schnell, J. L., Tilmes, S., Wild, O., Zhang, L., Ziemke, J., Brandt, J., Delcloo,  
1551 A., Doherty, R. M., Geels, C., Hegglin, M. I., Hu, L., Im, U., Kumar, R., Luhar, A., Murray,  
1552 L., Plummer, D., Rodriguez, J., Saiz-Lopez, A., Schultz, M. G., Woodhouse, M. T., and Zeng,  
1553 G.: Tropospheric Ozone Assessment Report: Assessment of global-scale model performance  
1554 for global and regional ozone distributions, variability, and trends, *Elementa: Science of the*  
1555 *Anthropocene*, 6, 10.1525/elementa.265, 2018.

1556 Zanis, P., Akritidis, D., Turnock, S., Naik, V., Szopa, S., Georgoulas, A.K., Bauer, S.E.,  
1557 Deushi, M., Horowitz, L.W., Keeble, J. and Le Sager, P., 2022. Climate change penalty and  
1558 benefit on surface ozone: a global perspective based on CMIP6 earth system models.  
1559 *Environmental Research Letters*, 17(2), p.024014.

1560 Zhang, Y. Q., Cooper, O. R., Gaudel, A., Thompson, A. M., Nédélec, P., Ogino, S. Y., and  
1561 West, J. J.: Tropospheric ozone changes from 1980 to 2010 dominated by equatorward  
1562 redistribution of emissions, *Nature Geoscience*, 9, 875–+, 10.1038/NGEO2827, 2016.

1563 Zhang, Y., West, J. J., Emmons, L. K., Flemming, J., Jonson, J. E., Lund, M. T., et al. (2021).  
1564 Contributions of World Regions to the Global Tropospheric Ozone Burden Change from 1980  
1565 to 2010. *Geophysical Research Letters*, 48, e2020GL089184.  
1566 <https://doi.org/10.1029/2020GL089184>

1567 Ziemke, J. R., Chandra, S., and Bhartia, P. K.: A 25-year data record of atmospheric ozone in  
1568 the Pacific from Total Ozone Mapping Spectrometer (TOMS) cloud slicing: Implications for

1569 ozone trends in the stratosphere and troposphere, *Journal of Geophysical Research -*  
1570 *Atmospheres*, 110, 10.1029/2004JD005687, 2005.

1571 Ziemke, J. R., Chandra, S., Duncan, B. N., Froidevaux, L., Bhartia, P. K., Levelt, P. F., and  
1572 Waters, J. W.: Tropospheric ozone determined from aura OMI and MLS: Evaluation of  
1573 measurements and comparison with the Global Modeling Initiative's Chemical Transport  
1574 Model, *Journal of Geophysical Research - Atmospheres*, 111, 10.1029/2006JD007089, 2006.

1575 Ziemke, J. R., Oman, L. D., Strode, S. A., Douglass, A. R., Olsen, M. A., McPeters, R. D.,  
1576 Bhartia, P. K., Froidevaux, L., Labow, G. J., Witte, J. C., Thompson, A. M., Haffner, D. P.,  
1577 Kramarova, N. A., Frith, S. M., Huang, L. K., Jaross, G. R., Seftor, C. J., Deland, M. T., and  
1578 Taylor, S. L.: Trends in global tropospheric ozone inferred from a composite record of  
1579 TOMS/OMI/MLS/OMPS satellite measurements and the MERRA-2 GMI simulation, *Atmos.*  
1580 *Chem. Phys.*, 19, 3257-3269, 10.5194/acp-19-3257-2019, 2019.

1581